One Earth

Article

Contrasting consequences of the Great Green Wall: Easing aridity while increasing heat extremes

Graphical abstract

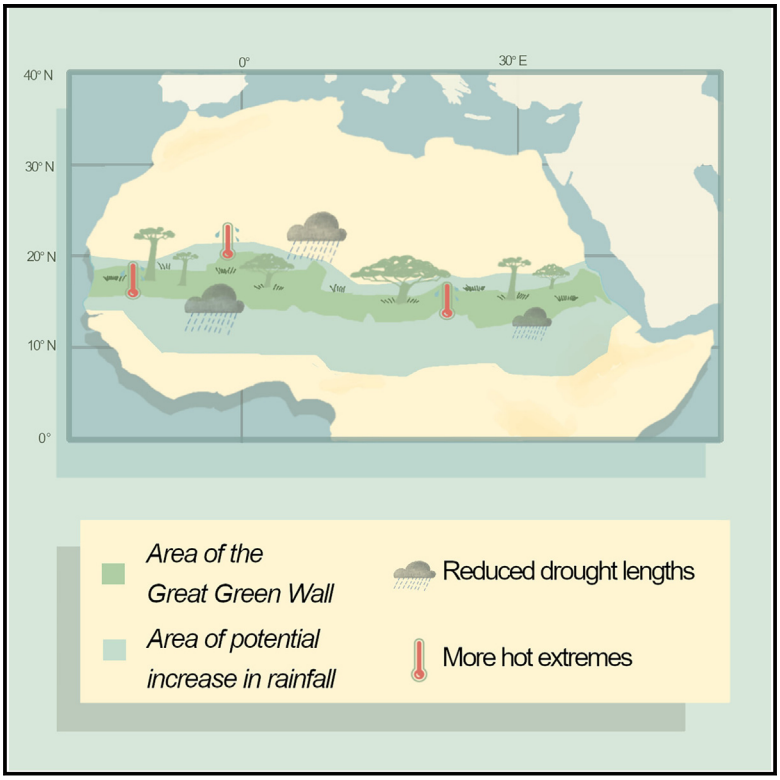

Highlights

- The GGW effectively reduces drought lengths
- While decreasing temperature in summer, the GGW causes warming in the other seasons
- The GGW leads to an increase in temperature extremes
- While water availability improves, the heat stress on local population worsens

Authors

Roberto Ingrosso,
Francesco S.R. Pausata

Correspondence

ingrosso.roberto@uqam.ca (R.I.),
pausata.francesco@uqam.ca (F.S.R.P.)

In brief

The Great Green Wall (GGW) initiative in Sahel aims to combat desertification but lacks a thorough understanding of its potential climate impacts. Our study considers multiple vegetation density and global warming scenarios. The GGW generally led to increased rainfall, reduced drought lengths, and cooler summer temperatures beyond its immediate borders. However, all scenarios show more extreme heat events. Understanding these diverse effects is crucial for policymakers to align the GGW goals with sustainable climate targets and mitigate potential regional repercussions.

Ingrosso & Pausata, 2024, One Earth 7, 455–472
March 15, 2024
https://doi.org/10.1016/j.oneear.2024.01.017

CellPress

One Earth

CellPress
OPEN ACCESS

Article

Contrasting consequences of the Great Green Wall: Easing aridity while increasing heat extremes

Roberto Ingrosso[1,2,*] and Francesco S.R. Pausata[1,*]
[1]Centres ESCER (Étude et la Simulation du Climat à l'Échelle Régional) and GEOTOP (Research Center on the dynamics of the Earth System), Department of Earth and Atmospheric Sciences, University of Québec in Montréal, Montréal, QC H2X3Y7, Canada
[2]Lead contact
*Correspondence: ingrosso.roberto@uqam.ca (R.I.), pausata.francesco@uqam.ca (F.S.R.P.)
https://doi.org/10.1016/j.oneear.2024.01.017

SCIENCE FOR SOCIETY Africa's Great Green Wall (GGW) initiative seeks to plant a wall of trees across the entire Sahel in an effort to hold back the expansion of the Sahara Desert and restore degraded land to the benefit of local communities. Although this geoengineering project has potential advantages, the extent to which the experiment will lead to a noticeable reduction in the intensity of droughts and heatwaves remains unclear. Without a deeper understanding of the potential climate impacts of the project, land restoration goals may not be achieved. Computer modeling that considers different GGW scenarios with different combinations of grasses and tree species, reveals that, while the project could increase rainfall and decrease drought duration, this would be accompanied by more extreme heat events in the pre-monsoonal season. Recognizing these diverse effects is essential for policymakers to align the GGW's goals with sustainable climate targets and mitigate potential regional repercussions.

SUMMARY

The Great Green Wall (GGW) is a multibillion-dollar African initiative to combat desertification in the Sahel. However, the potential climate impacts of the most recent GGW plan on northern Africa have not yet been adequately evaluated, raising concerns about unforeseen climate ramifications that could affect stability in northern Africa and undermine the goals of the initiative. Using a high-resolution (~13 km) regional climate model, we evaluate the climate impacts of four GGW scenarios with varying vegetation densities under two extreme emission pathways (low and high). Higher vegetation density GGW scenarios under both emission pathways show enhanced rainfall, reduced drought lengths, and decreased summer temperatures beyond the GGW region relative to the cases with no GGW. However, all GGW scenarios show more extreme hot days and higher heat indices in the pre-monsoonal season. These findings highlight the GGW contrasting climatic effects, emphasizing the need for comprehensive assessments in shaping future policies.

INTRODUCTION

The Sahel is a semi-arid transition region between the Sahara desert and the tropical savannah, and it has been considered one of the most important regional climate change hotspots throughout this century by means of a specific index defined as the Standard Euclidean Distance.[1,2] In the Sahara and Sahel regions, rainfall is closely linked with the intensity of the West African monsoon (WAM), which is crucial for the socio-economic stability of millions of people living there.[3] Severe droughts, most likely triggered by sea surface temperature (SST) anomalies[4–7] in synergy with natural vegetation processes, land-use changes, and anthropogenic emissions,[8,9] have ravaged the region in the last three decades of the 20th century.[10] To fight potential future droughts and land degradation, the Great Green Wall (GGW) has been conceived, based on the afforestation of about a 7,000-km-long stretch of degraded land from Senegal in West Africa to Djibouti in the East, with the objective of enhancing the hydrological cycle, increasing local rainfall in the region. In 2007, the GGW was officially adopted by the 11 founding Sahelian countries. The initial project of "a wall of trees" has been replaced by a more feasible initiative, an integrated ecosystem management approach that consists of a mosaic of different actions over an area within the 100 and 400 mm climatological annual isohyets.[11,12] Such a project has been designed to improve both environmental and socio-economic conditions

of the Sahelian countries.[13] The initiative has been selected among the first 10 World Restoration Flagships of the UN Decade on Ecosystem Restoration (https://www.decadeonrestoration.org/great-green-wall).

Recent research on the potential effect of the Sahelian green belt project or of more generic reforestation in northern Africa is limited.[14–19] Only a handful of studies using regional climate models (RCMs) have been performed to investigate the local impact of the reforestation of part or the entire Sahel.[15,16,18,19] The RCMs used by such studies are relatively coarse (i.e., 40–50 km) and may likely misrepresent the impact of reforestation on rainfall. The previous experiments were highly idealized and followed the original concept of a wall of trees, replacing the pre-existing vegetation with a uniform evergreen forest. However, the modeled area of the Wall was much broader than the 15-km width of the original initiative. In addition, the modeling of mesoscale convective systems that are responsible for 70% to 90% of the annual precipitation in the region[20–22] may have been misrepresented by the relatively low resolution of these experiments. Finally, the length of their experiments ranges from 7 (Diba et al.[16]) to 14 (Saley et al.[19]) years and, therefore, not sufficiently long to capture the full extent of the climatic changes associated with the GGW.

Here, we delve into the crucial aspect of understanding the potential climate impacts of the GGW, a fundamental need to guide stakeholders in formulating effective policies for the realization of the project. To achieve this, we employed a higher-resolution (13 km) climate model (Canadian Regional Climate Model [CRCM][23,24]) to portray a more accurate representation of the GGW initiative. We conducted sensitivity experiments under two distinct greenhouse gas (GHG) scenario pathways—the Representative Concentration Pathway 2.6 (RCP2.6) and RCP8.5[25]—encompassing four distinct GGW scenarios of varying vegetation densities (low, medium, high, and extreme) based on official documents of the GGW initiative[11] and the pronunciation of the "Commission de l'Union africaine and APA" in 2012 (see experimental procedures and Note S2 for details).

Our findings reveal contrasting effects of the GGW: higher vegetation density increases rainfall, reduces drought durations, and cools summer temperatures outside immediate borders. However, all scenarios exhibit amplified pre-monsoon heat extremes. These findings underscore the pivotal importance for policymakers to consider these multifaceted effects for effective environmental policy planning and comprehensive assessment of potential regional ramifications.

RESULTS

GGW enhances mean and extreme rainfall

Our model simulates no significant changes in rainfall over the Sahel during the 30-year averaged summer season (June to September [JJAS]) for both GHG emission scenarios (RCP2.6-only and RCP8.5-only), except for a dry anomaly over Senegal and southern Mauritania in the RCP8.5-only (Figure S2) relative to the present day (PD) experiment. This dry anomaly under the RCP8.5-only scenario is not found in the Regional Downscaling Experiment-Coordinated Output for Regional Evaluations (CORDEX-CORE) ensemble, which shows a moderately significant rainfall increase over the western Sahel (Figure S25A). CRCM/GEM4.8 seems to generally exhibit an underestimation of the mean precipitation compared with the CORDEX ensemble. However, this model bias should not affect the conclusions of this study as we focus on relative changes rather than absolute changes. Nevertheless, CRCM/GEM4.8 shows a good agreement with CORDEX in the extremes of the mean precipitation statistics (Figure S27), although CRCM presents a higher frequency of low rain rates compared with the CORDEX experiments. The CORDEX ensemble under RCP2.6-only does not show any particular change compared with PD (Figure S25C) although it shows a lower frequency of low rain rates compared with our model. For more details on the model evaluations and comparisons see experimental procedures.

When considering the GGW scenarios, a significant enhancement of the JJAS precipitation over a large area of the Sahel is simulated in three of the GGW experiments in both RCP2.6 and RCP8.5. While no significant change, apart from a few small pockets, is found in the GGW_{LOW}, GGW_{MED}, and GGW_{HIGH} experiments under both emissions, scenarios show a significant intensification in summer rainfall. Such intensification is more pronounced over the western Sahel, especially in GGW_{HIGH}, where an increase of 100 and 200 mm is present, corresponding to an increase of 50%–150% (Figures 1C–1F). Moreover, the GGW_{HIGH} scenario shows a further increase over central and southern parts of northern Africa, affecting the regions relatively far from the wall, such as southern Nigeria, Cameroon, and Central African Republic. An increase between 25 and 100 mm is also present over the northern and the eastern Sahel. In the extreme experiments (GGW_{EXT}), the signal is much stronger compared with the other scenarios, with a remarkable increase in precipitation over the entire northern Africa including the Sahara Desert. The increase in widespread rainfall ranges between 100 and 200 mm over the Sahelian region, representing an increase between 50% in the southern Sahel and 200% over the northern sections relative to the RCP-only experiments (Figures 1G and 1H). In addition, an increase between 250 and 500 mm is simulated in south-western Sahel. The aforementioned dry signal over the western Sahel in the RCP8.5-only simulation is partially or totally compensated in all experiments. The zonal means of daily precipitation over western Africa for the GGW_{HIGH} and GGW_{EXT} indicate that the effect of the GGW is not confined to the summer season but also extends into spring and fall (Figure S3). Furthermore, a strengthening of the WAM south of the GGW region is simulated, bringing more precipitation outside the project area as well. A significant increase of about 1 mm/day in these GGW scenarios is present over the western Sahel from April to November compared with RCP-only projections, with peaks above 3 mm/day in August for the GGW_{EXT} simulation under the RCP2.6 pathway (Figure S3D). However, the strengthening of the WAM—more pronounced in the second half of the summer in both GGW_{HIGH} and GGW_{EXT} experiments—is not associated with a notable lengthening of the monsoon season. While in the RCP8.5-only (but not in RCP2.6-only) experiment, the monsoon season is significantly longer (11 days, Figure S3F) than in the PD, no significant differences are detected between the RCPs-only and the more extreme GGW scenarios.

The positive rainfall anomalies associated with the presence of the GGWs are also reflected in a change in extreme events, decreasing the drought length and increasing the number of

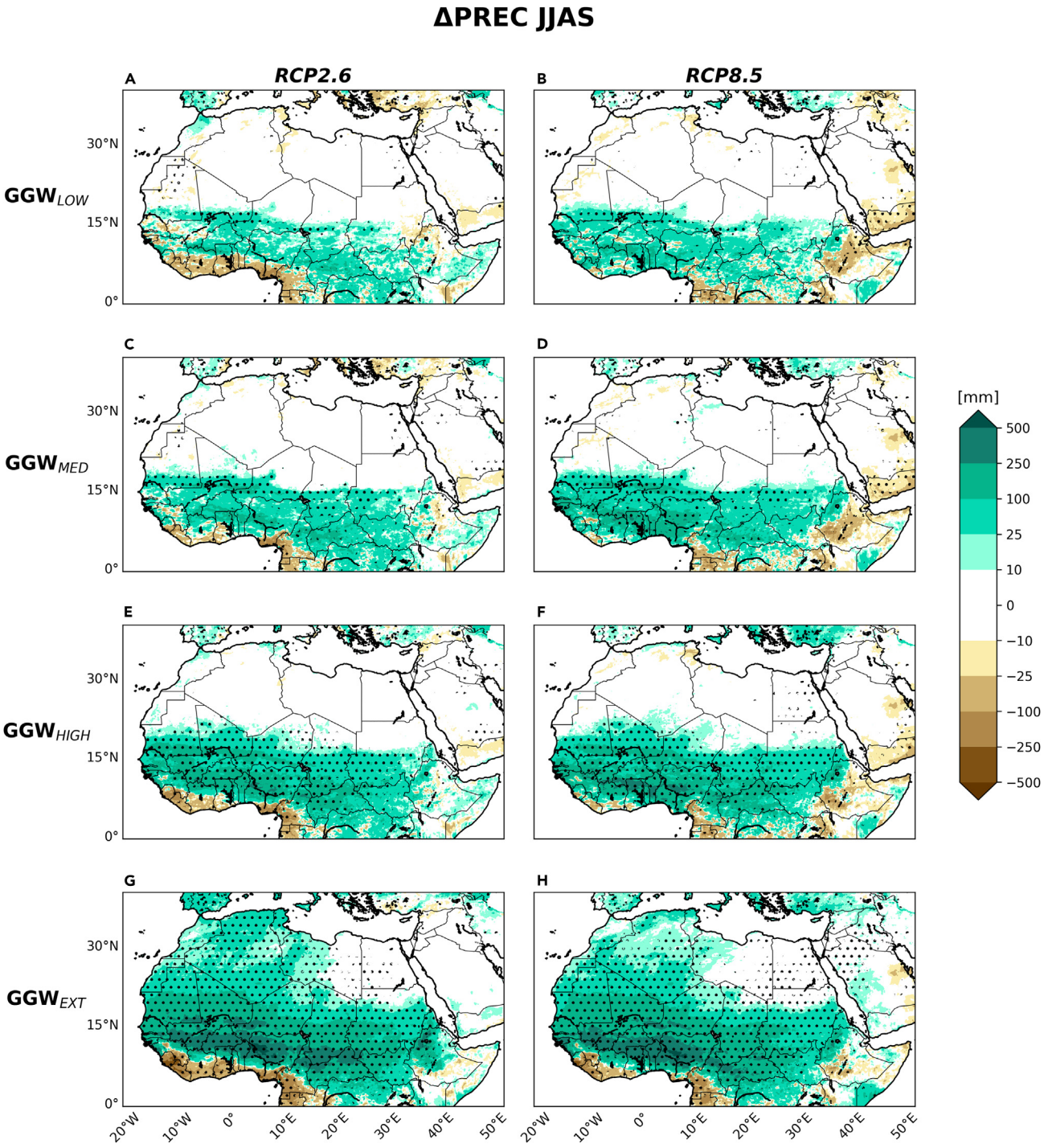

Figure 1. Summer rainfall changes in northern Africa

Changes in precipitation during summer (June to September [JJAS]) for (A and B) GGW_{LOW}, (C and D) GGW_{MED}, (E and F) GGW_{HIGH}, and (G and H) GGW_{EXT} scenarios relative to the standard RCP2.6 (left) and RCP8.5 (right) pathways. Dots indicate values that are significantly different at the 5% significance level using a local (grid-point) Wilcoxon signed-rank test.

rainy days and the intensity of rainy events. In particular, the RCP-only experiments do not show any notable differences relative to PD in terms of consecutive dry days (CDDs) (Figures 2B and 2C). Similar results with no clear changes in CDDs are shown by several studies, with the exception of a modest signal over the western Sahel.[26–28] Opposite CDD changes considering different climate models such as the Coupled Model Intercomparison Projects 5/6 (CMIP5/6) and CORDEX ones are found

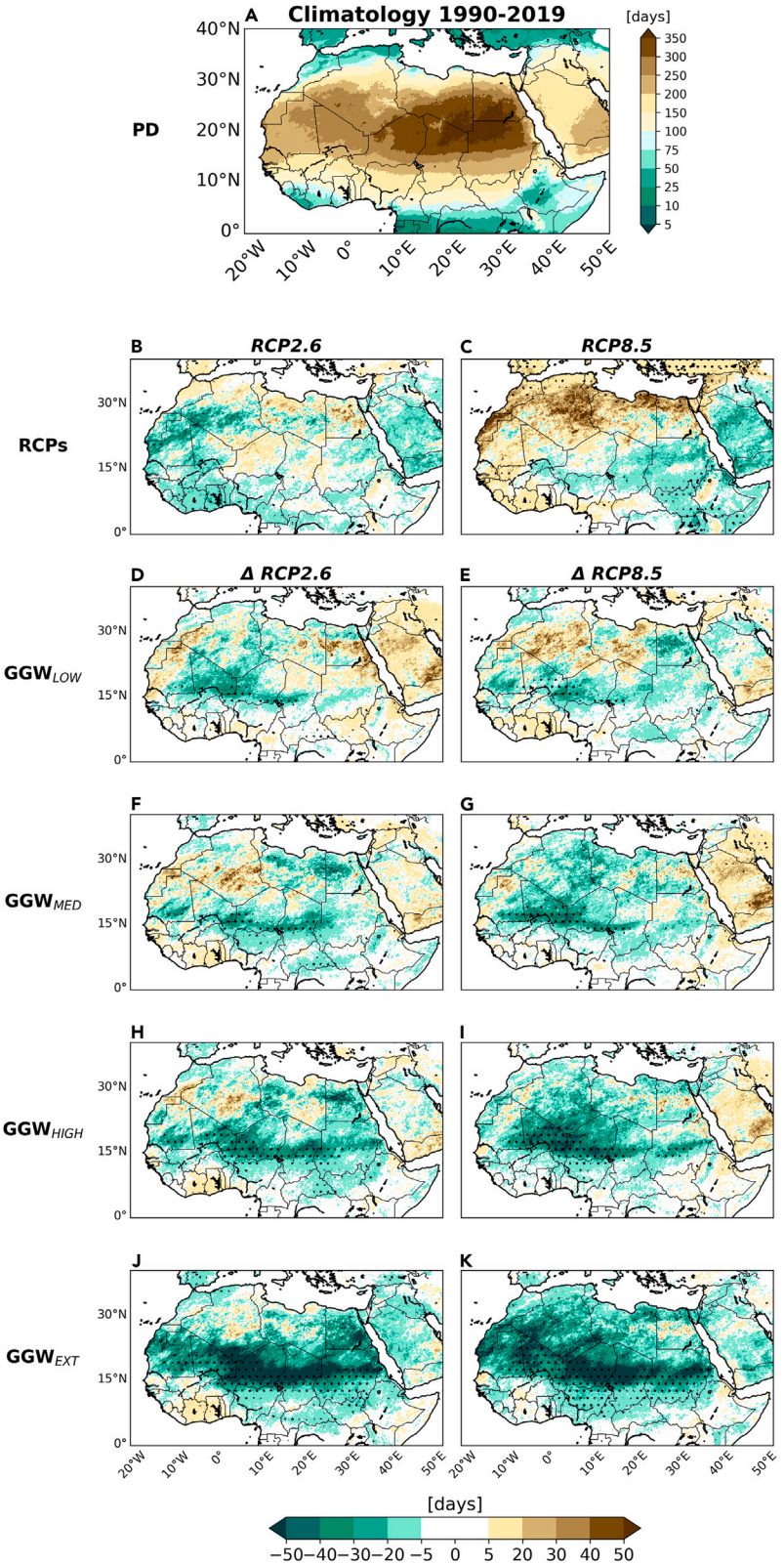

Figure 2. Annual consecutive dry days

(A) Climatological annual consecutive dry days (CCDs) for the present day (PD) experiment and its changes during summer (JJAS) for (B and C) RCP scenarios relative to the PD experiment, and (D and E) GGW_{LOW}, (F and G) GGW_{MED}, (H and I) GGW_{HIGH}, and (J and K) GGW_{EXT} scenarios relative to the standard RCP2.6 (left) and RCP8.5 (right) pathways. Dots indicate values that are significantly different at the 5% significance level using a local (grid-point) Wilcoxon signed-rank test.

by Dosio et al.[29] Finally, the CMIP6 models presented in the WGI-AR6 report[30] show a high model agreement in CDD decrease over central and western Sahel between 5 and 15 days in the 4°C global warming scenario. Although not significant, due to the high variability of the index in our experiments, we found a CDD decrease up to 20 days. A potential limitation in detecting CDD change in the future could also be associated with the convection parametrization as highlighted by Kendon et al.,[31] which shows better performance of a convection-permitting model at 4.5 km horizontal resolution compared with a convection-parameterized model at 25 km resolution. The GGW scenarios exhibit a significant decrease over the central Sahel, with differences depending on the level of vegetation density. The GGW_{LOW} scenario shows significant CDD changes of up to −40 days under both emission pathways between Mali and Niger (Figures 2D and 2E). A similar, but broader pattern is shown in the GGW_{MED} scenarios (Figure 2), where the CDD decrease reaches parts of Mauritania and Chad. In the GGW_{HIGH} and GGW_{EXT} experiments, the change involves a wider area up to −52 days in the central Sahel (Figures 2H–2K). Given that the region experiences lengths of about 150 CDD in the southern Sahel and 300 CDD in the northern Sahel a year in the PD simulation (Figure 2A), such changes are remarkable. They indeed correspond to a shortening of droughts between 5% and 20% in the GGW_{LOW}, GGW_{MED} scenarios and up to 40% in the GGW_{HIGH} and GGW_{EXT} experiments.

The increased vegetation also leads to a significant increase in rainy days (days with daily precipitation higher than 1 mm, R1mm), between 50% and 150% over the whole area of the project in all GGW experiments, except for the eastern Sahel in the GGW_{LOW} scenario (Figure S4). Changes of more than 14 days in the GGW_{LOW} and more than 18 days for the other GGW scenarios compared with the RCP-only experiment are simulated over the project domain, canceling out the R1mm decrease over the western Sahel under the RCP8.5 scenario. No significant change in very wet days (R95p, Figure S5) and 5 consecutive day rainfall maximum (RX5) (Figure S6) is associated with the GGW_{LOW} and GGW_{MED} experiments except for a few limited areas in the latter. Changes in R95p and RX5 over central and western Sahel in the GGW_{HIGH} and GGW_{EXT} experiments are significant, with an increase in both indexes of up to 100 mm compared with RCP-only projections. Once again, this increase in precipitation is more intense and widespread in the GGW_{EXT} experiments, with an anomaly in the R95p and RX5 indexes above 125 mm over the south-western Sahel relative to RCP-only simulations.

Potential mechanisms behind the precipitation changes

The RCP8.5-only experiment does show a significant increase of the shallow convection just before the surface convergence zone with no evident latitudinal displacement of the convergence system (Figure S7C). The RCP2.6-only experiment shows no significant change in the regional circulation compared with the PD simulation (Figures S7B and S8B), which is consistent with no increase in precipitation in this experiment (Figure S2A). However, no significant change of the tropical easterly jet and only a light strengthening of the African easterly jet (AEJ) (Figure S8C) is simulated. Such conditions are not favorable to increased precipitation.[32] On the contrary, a northward expansion of the monsoon flux is detected in all GGW experiments with a stronger and more pronounced penetration of the WAM in the more extreme GGW scenarios compared with the PD and RCP-only experiments (Figures S7H–S7K). In such GGW experiments, much deeper convection relative to RCP-only experiments develops, reaching the mid-troposphere (500–600 hPa) at 15°N–18°N, explaining the northward expansion of the rainfall (Figure 1). In the GGW_{EXT} simulation, the enhanced deep convection also occurs further south (10°N), coherently with the increase in precipitation over the whole of northern Africa. Following the monsoon expansion, the northward component of the monsoon and the southward component of Harmattan winds weaken as the density of vegetation increases (and consequently the precipitation), suggesting a waning of the shallow meridional circulation, which plays a role in the amount of rainfall in the Sahel.[33] This weakening may partially be due to the increase in surface roughness related to replacing desert and bare soil with trees and shrubs (Table S5). The monsoon northward expansion is associated with a proportional increase of the easterly jet at higher altitudes and a decrease of the AEJ, going from almost no changes in the GGW_{LOW} simulations (Figures S8D and S8E) to large and significant changes in the GGW_{EXT} experiments (Figures S8F–S8K). At the synoptic scale, a remarkable increase in the African easterly waves (AEWs), which are responsible for most of the precipitation over the Sahel, is simulated in the presence of the GGWs under both emission pathways with a clear increase over the whole southern part of western Africa, peaking over the Atlantic Ocean at around 10°N (Figure S9). Such an increase in AEWs, combined with the change in the easterly jets, leads to more precipitation over the area due to increased potential vorticity.[34] The increase in AEWs may be triggered by the increase in heat release associated with the increase in convection[35] and enhanced by positive feedback with the convection itself.[22]

The large increase in the moisture flux and total moisture flux convergence (TMFC) in the RCP-only experiments compared with the PD experiment (Figure S12C; Table S4) over the region is not associated with increased precipitation in these experiments. This change does not indeed trigger any significant modification in deep convection (Figures S7B and S7C). In the GGW experiments, a slight increase in the TMFC compared with the RCP-only experiments is found. The changes in vegetation density in the GGW only modestly perturb the TMFC. In relative terms, the main difference compared with the RCP-only experiments is an increase in evapotranspiration due to the GGW (Figure S11; Table S4). This is proportional to the vegetation density and allows deeper and more effective convection (Figure S7), leading to an overall increase in precipitation in the region. This suggests a fundamental role of evapotranspiration in the GGW-induced changes in rainfall, with the increase in the TMFC giving a limited contribution. Consequently, land-atmosphere interactions through vegetation and albedo feedbacks[36,37] seem to play a crucial role in triggering the change in the WAM dynamics rather than large-scale circulation change associated, for example, with anomalous SST as in the RCP8.5-only experiment.

GGW impacts on temperature

Surface temperature in the Sahel is characterized by a bimodal pattern of the annual cycle with two maxima before and after

the rainy summer season. The hottest season corresponds to the boreal spring, just before the onset of the WAM, which then causes a temperature decrease. The RCP2.6-only and RCP8.5-only simulations show highly significant warming over the whole of northern Africa during the monsoon season (JJAS, Figures 3A and 3B). In particular, in the Sahel, the warming ranges between 0.5°C and 1°C in the RCP2.6-only experiment and over 4°C warming region, with a peak of more than 5°C over the eastern side, in the RCP8.5-only scenario, in overall good agreement with the CORDEX-CORE ensemble (Figure S26, for more details, see Note S1).

When the impact of the GGW is considered, no significant JJAS change in the mean temperature is shown in the GGW_{LOW} scenario compared with the RCP-only simulations (Figures 3C and 3D), whereas a cooling over the central-western Sahel with a peak of up to 1.5°C is simulated in the GGW_{MED} experiment (Figures 3E and 3F). The GGW_{HIGH} scenario shows a significant decrease in temperature over a much wider area than the GGW domain itself, a clear consequence of the strengthening of the WAM (Figures 3G and 3H). This cooling ranges between −0.5°C and −1°C for both emission scenarios, with a peak larger than −1°C in central Mali and southern Niger. These anomalies are doubled and extend well into the Saharan desert when considering the GGW_{EXT} experiment (Figures 3I and 3J). In the GGW_{HIGH} experiment under the RCP2.6 pathway, the GGW cooling largely offsets the warm season (JJAS) warming signal over the area (Figure S16B) caused by the increased GHG concentrations. This cooling is a consequence of increased cloudiness (Figure S13B, bottom), which reduces the amount of sunlight reaching the surface, and rainfall, which enhances evaporation. Moreover, the increase in evapotranspiration associated with the higher vegetation density (Figure S11) may also play a role in the simulated temperature decrease in summer. Hence, the potential warming associated with the reduced albedo is overshadowed by the cooling from evapotranspiration and increased cloud cover. On the contrary, warming is present during the pre-monsoon season (March to May, Figure S17). While the summer cooling extends well beyond the boundaries of the GGW, the warming is confined to the area in which the vegetation change has been applied and ranges between −0.25°C and −1°C with a peak over 1°C in central Mali and southern Niger (Figures S17A–S17F). The warming signal in the GGW_{EXT} is wider—consistent with a larger area of the wall—and stronger compared with the other GGW experiments—and is generally between 0.5°C and 1.5°C with several peaks shy of 2°C in different parts of central Sahel (Figures S17G and S17H). Such warming is a clear consequence of the decrease in albedo associated with the vegetation cover (Figure S15). Furthermore, the evaporative cooling is reduced during the dry season due to the dry soil, causing the plants in the region to transpire less than later in the season.

A cooling during the monsoonal season and a warming during the pre-monsoonal season show that the GGW produces contrasting seasonal impacts over the region. This effect can be clearly seen by looking at the annual cycle of maximum and minimum daily temperature over the Sahel, where the warming is also present during the fall and the winter (Figure S18A). The temperature range between the climatological hottest day of the year in spring and the summer coldest day increases by about 0.4°C in GGW_{MED}, and 1°C in GGW_{HIGH} and GGW_{EXT} scenarios relative to the RCP-only experiments. The summer minimum temperature in the GGW_{EXT} experiment under the RCP2.6 pathway presents values comparable with the PD (Figure S18B), increasing the seasonal temperature range between spring maximum and summer minimum temperature. Furthermore, in spring the minimum temperature also increases due to the higher heat capacity of grass, shrubs, and trees compared with bare soil and desert, especially in the more extreme GGW experiments relative to RCPs-only.

In terms of temperature extremes, the annual hottest day (TXx) and coldest day (TNn) show an increase of about 4°C over the Sahel with peaks above 5°C in the western Sahel for TNn in the RCP8.5-only experiment relative to the PD (Figure S19). The GGW experiments show significant changes in temperature extremes compared with the RCP-only scenarios over the area of the project (Figures 4 and S20) with an impact that is wider as we move from low to extreme cases. The increase in temperature of the coldest day of the year (TNn) reaches up to more than 1.5°C over the central Sahel in the medium to extreme vegetation density experiments (Figures 4A–4D). The temperature increase of the hottest day (TXx) is instead smaller ranging between 0.3°C and 0.9°C with peaks of 1.2°C in central Sudan (Figures 4E–4H). The number of tropical nights (TR20) rises from 10 (GGW_{LOW}) to up to more than 25 (GGW_{MED}, GGW_{HIGH}, and GGW_{EXT}) over the GGW area under both emissions scenarios (Figures 4I–4L and S20I–S20L). For the GGW_{EXT} experiment, the results show a wider area affected by the change in TXx (Figures 4H and S20H) compared with the other GGW scenarios, consistent with the larger vegetated area. Generally, the increase in the temperature extremes is primarily due to the decrease in albedo and increase in relative humidity related to the presence of the GGW: more solar radiation is absorbed during the day (lower albedo), whereas less heat is released at night (higher humidity). During the monsoonal season, the increase in cloudiness and precipitation favors a decrease in mean temperature as mentioned before. During the spring, a much smaller increase in clouds (Figure S14) and rainfall compared with the summer does not compensate for the increased solar radiation absorbed by the changes in surface albedo. The minimum temperatures also increase due to an overall humidification associated with the vegetation changes, which reduces nighttime cooling. In the GGW_{LOW} scenario no significant cooling in the mean and extreme daily temperature during the summer is simulated, whereas a clear increase in both mean and daily extreme temperature is simulated during the pre-monsoonal season.

A less arid Sahel

To detect a potential change in water availability over northern Africa associated with the GGW, we adopted the De Martonne aridity index (AI_{DM}) (De Martonne[38]). The AI_{DM} is a simple and efficient index that is defined as a function of the annual mean precipitation and temperature (for details, see experimental procedures), with lower (higher) values indicating higher (lower) levels of aridity. We also highlight the AI_{DM} change of the seven most important Sahelian cities (Figure 5). In the PD experiment, AI_{DM} clearly shows the abrupt transition from desert to slightly arid conditions, with a prevalence of semi-arid/arid climate over the entire Sahel. No significant changes in the region are

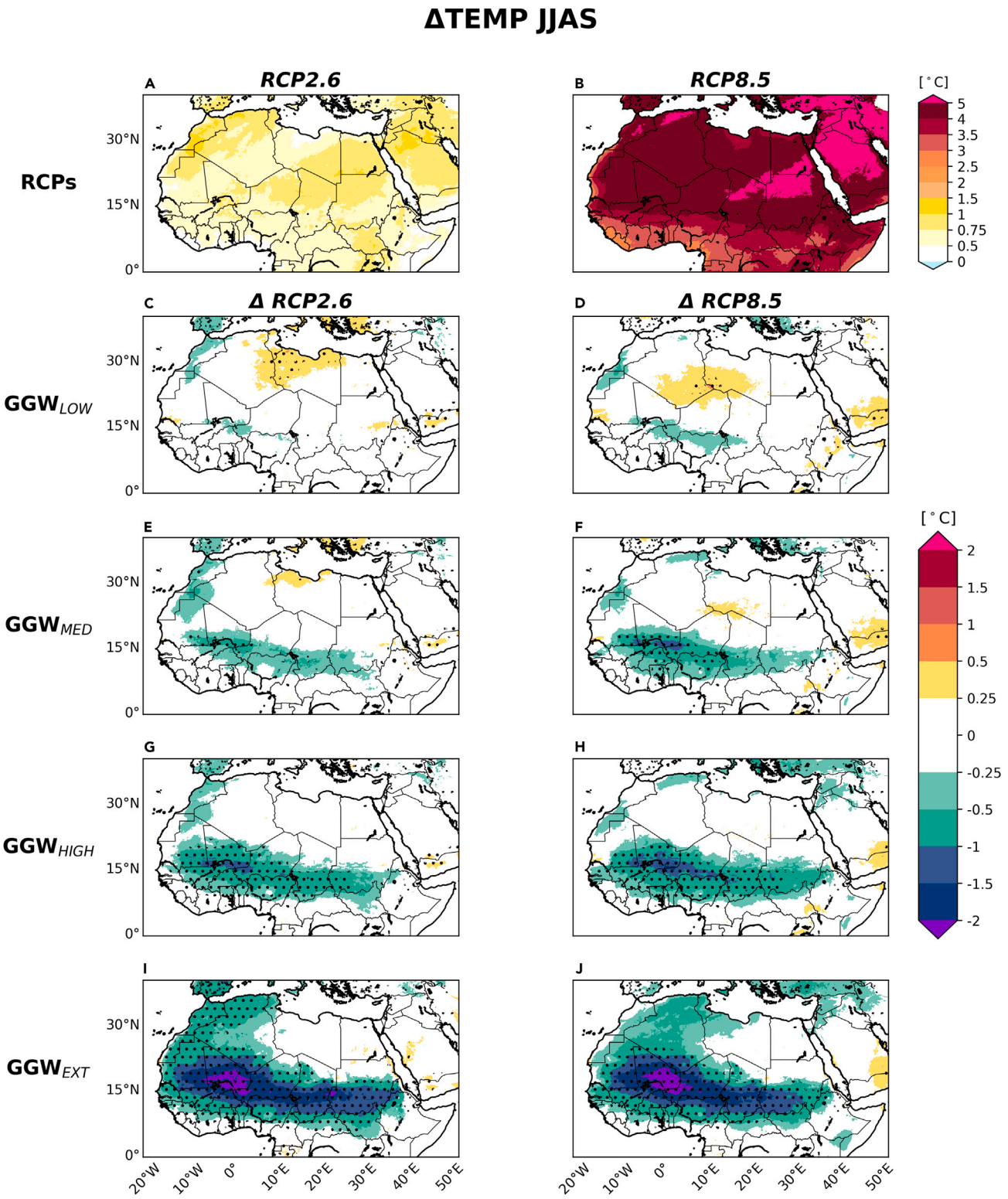

Figure 3. Mean temperature changes during JJAS

Changes in mean temperature during summer (JJAS) for (A and B) RCP scenarios relative to the PD experiment and (C and D) in the GGW_{LOW}, (E and F) GGW_{MED}, (G and H) GGW_{HIGH}, and (I and J) GGW_{EXT} scenarios relative to the standard RCP2.6 (left) and RCP8.5 (right) pathways. Dots indicate values that are significantly different at the 5% significance level using a local (grid-point) t test. In (A) and (B) all areas show significant differences (no dots shown).

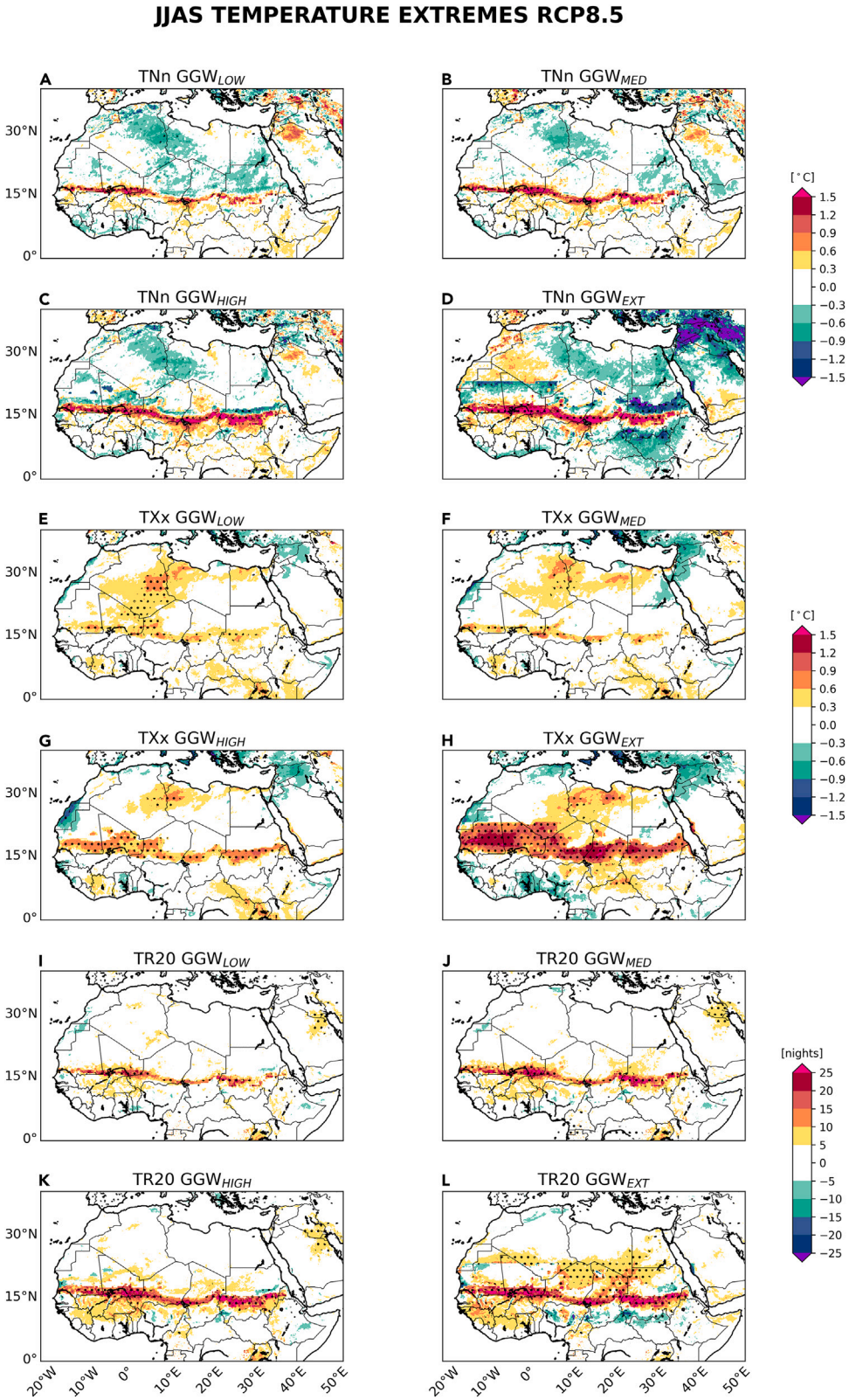

Figure 4. Change in the hottest and coldest day of the year and number of tropical nights

Change in the annual coldest day of the year (TNnx) for (A) GGW_{LOW}, (B) GGW_{MED}, (C) GGW_{HIGH}, and (D) GGW_{EXT} scenarios relative to the standard RCP8.5 pathway. (E–H) Same as (A–D) but for the hottest day of the year (TXx). (I–L) Same as (A–D) but for tropical nights (number of nights with daily minimum temperature above 20°C, TR20). Dots indicate values that are significantly different at the 5% significance level using a local (grid-point) t test.

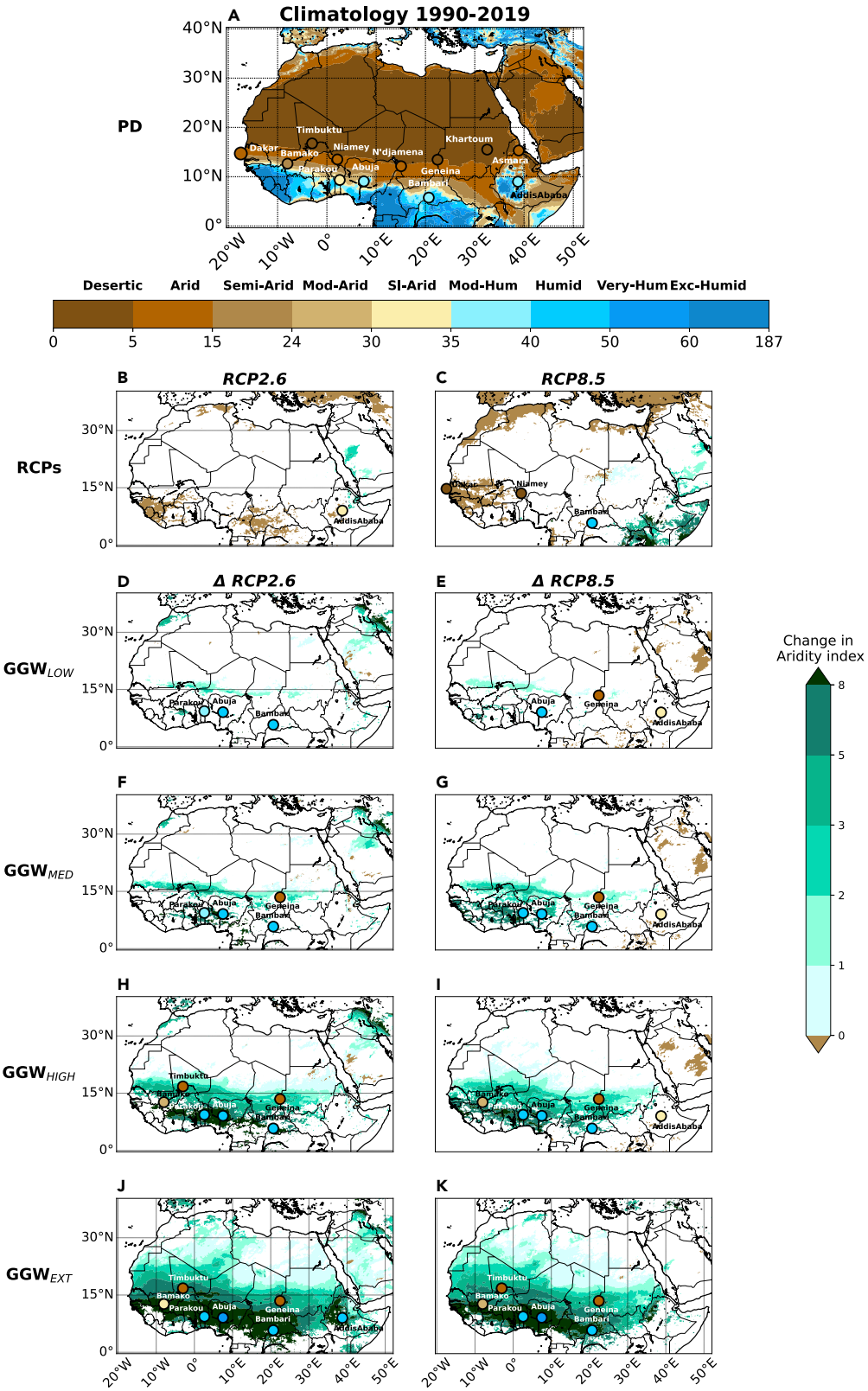

(legend on next page)

found in the reference future projections, except for an expected slight decrease in the AI_{DM} over the western Sahel (Figures 5B and 5C), concurrent with the simulated precipitation deficits (Figure S2B).

When the GGW is considered, a significant AI_{DM} increase over central and western Sahel is present for the GGW_{MED}, GGW_{HIGH}, and GGW_{EXT} scenarios, even doubling over northern Sahel in the last two cases (Figures 5F–5K). In the GGW_{LOW} experiment, a weak significant change in AI_{DM} is simulated, especially in the southern part of Mauritania, Mali, and Niger (Figures 5D and 5E). Changes in the aridity conditions among the areas of the most important cities in the region have been assessed. Parakou in Benin is the city that shows the largest benefits moving from slightly arid to moderate humid conditions in the GGW_{LOW} and GGW_{MED} scenarios under the RCP2.6 pathway. It becomes humid in the GGW_{MED} scenario under the RCP8.5 pathway and in both RCP pathways for GGW_{HIGH} and GGW_{EXT} experiments. Bamako in Mali sees a shift from a semi-arid to moderately arid climate in the GGW_{HIGH} and GGW_{EXT} experiments and even to slightly arid in the GGW_{EXT} scenario under the RCP2.6 pathway. Geneina, in West Durfur (Sudan), moves from desertic to arid conditions in all GGW experiments, except the GGW_{LOW} under the RCP2.6 pathway. This wet signal reaches the southern parts of northern Africa, with Abuja, the capital of Nigeria, moving from moderate humid to humid conditions in all experiments, except in the GGW_{EXT} scenario, where it jumps to very humid conditions. Even part of the Central African Republic is touched by this decrease in the aridity conditions, with the city of Bambari moving from moderately humid to humid AI_{DM} values in the RCP8.5-only pathway and almost all GGW scenarios, except GGW_{LOW}, under the RCP8.5 pathway. Timbuktu in Mali, currently classified as desert, shifts to an arid climate in all GGW_{EXT} experiments and the GGW_{HIGH} scenario under the RCP2.6 pathway. Dakar in Senegal does not show any change in AI_{DM} in the GGW experiments; however, the presence of the GGWs cancels out the dry anomaly associated with the increase in GHGs, avoiding the possibility of approaching desert-like conditions, as the AI_{DM} value is just shy of aridity level in the RCP8.5-only experiment. Although a widespread increase of AI_{DM} is displayed over the Sahel and sub-Sahel region, it is not sufficient to cause a transition to a wetter AI_{DM} category in the other cities.

Increase in heat stress for the local population

While our previous analysis shows a decrease in the aridity conditions over most of the Sahel and sub-Sahelian regions associated with the GGW, higher temperature during the premonsoonal season together with higher humidity driven by increased evapotranspiration may cause more intense heat stress on the local population. To investigate such potential changes in human discomfort, we calculate the heat index (HI) or apparent temperature, which is a metric based on temperature and relative humidity, allowing us to assess the level of heat stress on the population. The HI is a measure of the temperature that the human body feels. An HI above 37.8°C–39.4°C (100°F–103°F) is considered dangerous for the local population, whereas an HI above 49.4°C–51.1°C (121°F–124°F) is assessed as extremely dangerous (https://www.weather.gov/ama/heatindex).

In the RCP8.5-only scenario, the heat index significantly increases over the whole of northern Africa relative to the PD simulation with a surge in the number of days above the 75th percentile (between 200 and 250), half of which is above the 95th percentile (between 100 and 175 days) over the Sahel (Figures 6A and 6B). The only exception is represented by an area between central Ethiopia and southern Eritrea, which does not show any significant change. In the GGW experiments, we also considered the number of days above the PD 75th and 95th percentiles and calculated their change relative to the RCP-only experiments. The HI change reflects the same pattern seen before for the temperature anomalies with an increase of HI extremes compared with the RCP8.5-only experiment that is proportional to the vegetation density (Figures 6C–6J). In the GGW_{LOW} experiment under the RCP8.5 scenario a peak increase of 20 days above the 75th and 95th RCP8.5-only percentiles is simulated between southern Niger and southern Mali (Figures 6C and 6D). The GGW_{MED} scenario shows an increase between 20 and 40 days compared with the RCP8.5-only experiment over a wider area that reaches southern Mauritania and Chad (Figures 6E and 6F). As expected, the largest increases are simulated in the GGW_{HIGH} and GGW_{EXT} scenarios. The GGW_{HIGH} shows intensification in HI extremes between 30 and 40 days in the south regions of Mauritania, Niger, and Mali relative to the RCP8.5-only experiment (Figures 6G and 6H)), while between 20 and 30 days in central and eastern Sahel. Compared with RCP-only experiments, in the GGW_{EXT}, the number of HI extreme days increases by more than 50 days over Mauritania and Mali, with central and eastern Sahel experiencing up to 40 days in several areas (Figures 6I and 6J). Especially in these highest vegetation density experiments, northern Africa generally shows a significant increase in extreme HI days with some exceptions, especially over Morocco, the Horn of Africa and the coastline along the Gulf of Guinea that experience a decrease in extreme HI days compared with the standard RCP8.5 scenario. The impact of global warming in the high emission scenario on the Sahelian HI can be clearly seen in the shift of the HI value distribution under RCP8.5 (Figure S22, red curve): both mean and variance increase, leading to a significant shift of the right tail of the HI distribution (values above the 95th percentile). The presence of the more extreme GGWs further increases the variance and the skewness of the curves, causing even more extreme HI values compared with the RCP8.5-only/RCP2.6-only experiment (Figure S22, light and dark green curves) across the entire

Figure 5. De Martonne aridity index

(A) Climatology of the De Martone aridity index (AI_{DM}) for PD. Change in AI_{DM} for (B and C) the RCPs relative to PD experiment, and for (D and E) the GGW_{LOW}, (F and G) the GGW_{MED}, (H and I) GGW_{HIGH}, and (J and K) GGW_{EXT} scenarios relative to the standard RCP2.6 (left) and RCP8.5 (right) pathways. Sl-arid, mod-Hum, and Exc-Hum indicate slightly arid, moderately humid, and excessively humid conditions. Dots indicate the associated AI_{DM} of that specific city. Only statistically significant change at the 5% significance level is shown, using a local (grid-point) Wilcoxon signed-rank test. In the maps of differences, only the cities characterized by change in the index are shown.

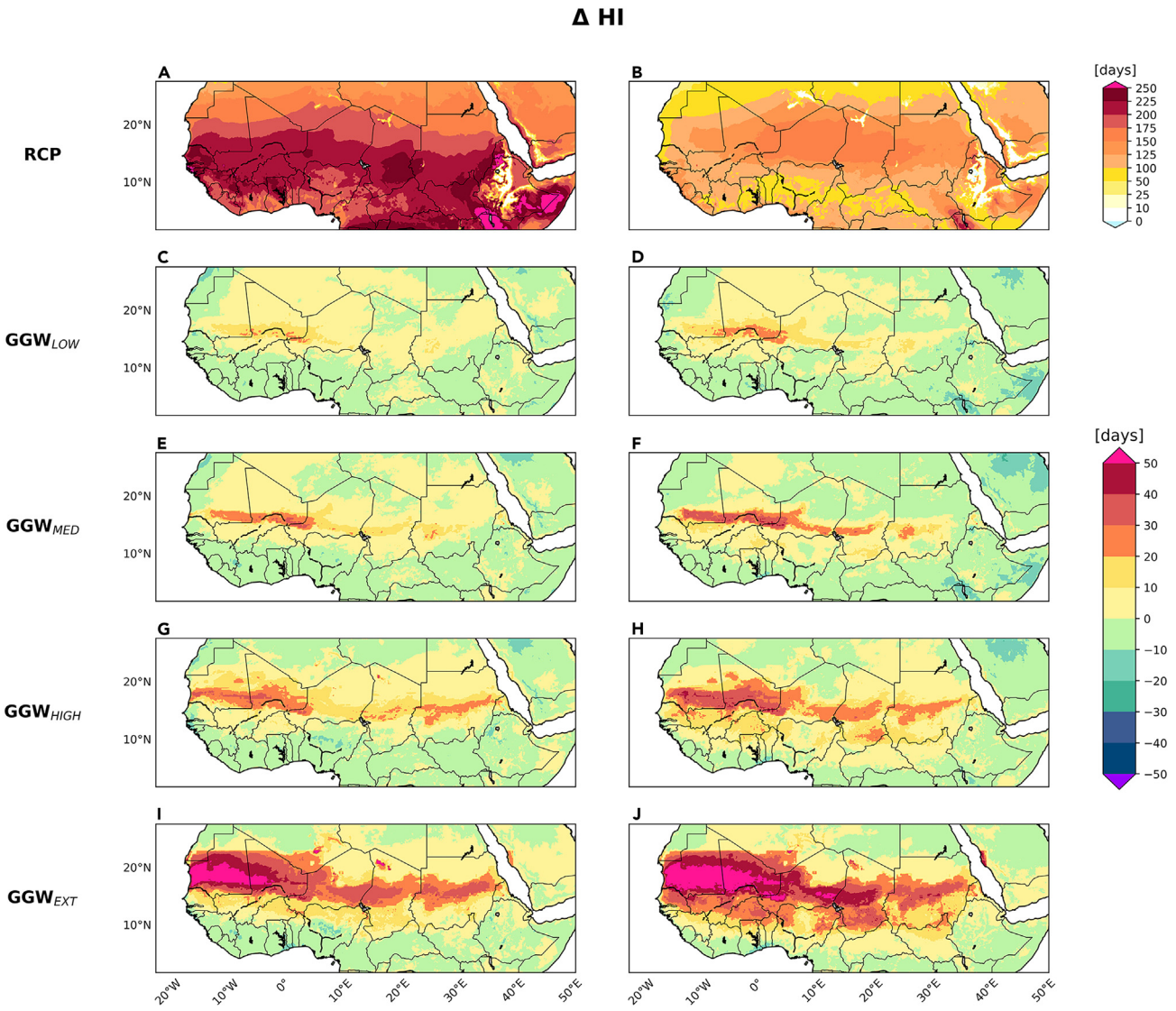

Figure 6. Heat index

(A and B) Annual change in the number of days with a heat index (HI) higher than PD 75th (left) and 95th (right) percentile for RCP8.5-only. Difference in number of days with HI higher than PD 75th (left) and 95th (right) percentile for (C and D) GGW$_{LOW}$, (E and F) GGW$_{MED}$, (G and H) GGW$_{HIGH}$, and (I and J) GGW$_{EXT}$ relatively to RCP8.5-only experiment.

Sahel except for the easternmost part (see Sahel and Sahelian cities distributions in Figure S23). Such an increase in HI due to the GGW is mostly a reflection of albedo and humidity changes associated with the vegetation. However, contrary to the increase in extreme temperature (Figures 4 and S20), the changes in HI extend well outside the GGW due to an increase in humidity, evaporation (Figure S10), and evapotranspiration (Figure S11) over a much wider area compared with the project. In the RCP2.6 scenario, the effect of the GGW on the HI seems to strengthen as the number of days exceeding the PD 75th and 95th percentiles increases by more than 50 compared with the RCP2.6-only experiment. In the GGW$_{EXT}$, these peaks cover almost the whole Sahel (Figures S21C–S21J). HI distribution under RCP2.6 also shows a shift in the right tails for the whole Sahel (Figure S22) and the Sahelian cities (Figure S24), apart from Addis Ababa (Ethiopia) and Asmara (Eritrea), in the eastern Sahel. However, as expected, the change in mean and variance are much more limited than in the RCP8.5 scenario.

DISCUSSION

Greening projects of the Sahel aim to improve the socio-economic conditions of one of the poorest regions in the world; however, they are constrained by anthropogenic-induced changes and natural climate variability, water scarcity, and limited habitable conditions. While the original and generalized idea of GGW relied on the image of a literal green wall along the Sahel, the current project has evolved into a broader integrated ecosystem management approach based on dryland regulation,

regeneration of vegetation, water retention, and ecosystem conservation.[39]

This study investigates potential changes in rainfall and temperature and their extremes over northern Africa associated with the development of the GGW initiative under two future emission scenarios (RCP2.6 and RCP8.5). We use a higher-resolution atmospheric RCM (~13 km) and a more realistic experimental design compared with previous studies,[16,18,19] offering a set of different vegetation density scenarios for the GGW. Our analysis shows no significant increase in mean precipitation in the GGW_{LOW} experiment compared with the standard RCP scenarios without vegetation changes. On the other hand, the GGW_{MED} and GGW_{HIGH} experiments reveal an increase in mean summer rainfall ranging between 25 and 200 mm over the western Sahel, and between 25 and 100 mm over the eastern Sahel, respectively. An increase of 100–200 mm over the whole Sahel is simulated in the GGW_{EXT} scenario, with peaks between 250 and 500 mm over the southwestern Sahel (Figure 1). The negative anomaly over Senegal and southern Mauritania in the RCP8.5-only projections relative to PD is canceled out in these experiments. Furthermore, the positive rainfall anomalies extend well beyond the domain of the GGW, in particularly south of the GGW in the GGW_{HIGH} scenario and the whole of northern Africa in the GGW_{EXT} experiments. In terms of extreme events, the GGW experiments exhibit a clear decrease in the length of dry spells (CDD) between −5% and −15% in the GGW_{LOW}, GGW_{MED}, and GGW_{HIGH} scenarios, and up to −25% in the GGW_{EXT} case (Figure 2). The areas affected by this change broaden proportionally to the increase in vegetation density. A significant increase in rainy days between 50% and 150% characterizes the whole area of the project in all experiments (Figure S4). However, the areas affected by such changes depend on the vegetation density and the intensification of heavy rainfall events (RX5D and R95p) is only simulated in the GGW_{HIGH} and GGW_{EXT} scenarios (Figures S5 and S6). These results suggest that vegetation density is crucial in determining the effects of the GGW on rainfall, with small or negligible impacts for the low vegetation case and clear, significant impacts for the high and extreme GGW scenarios.

Previous works[16,18] showed a larger increase in rainfall (up to 4 mm/day); however, in these studies, the vegetation was replaced by forest over a wider area than our modeled GGW. On the other hand, changes in climate extremes are generally more pronounced in our study compared with previous studies,[16,19] likely due to the length of their experiments (7–14 years), which does not fully capture the amplitude of climate variability.

In terms of temperature changes associated with the GGW, we find a different response over the Sahel depending on the period of the year. In summer, a temperature decrease ranging between 0.25°C and 0.5°C and between 0.5°C and over 2°C is simulated for the GGW experiments relative to the RCP-only scenarios with no vegetation changes with the only exception of the GGW_{LOW} in which no significant change is simulated (Figure 3). In the GGW_{HIGH} and GGW_{EXT}, this cooling extends over a wider area compared with the project domain as a consequence of the increased cloud cover and evaporation associated with the strengthening of the WAM. On the other hand, an albedo-induced increase in temperature confined to the GGW domain characterizes the other seasons, especially during the pre-monsoonal period, when the highest temperatures are reached in the region. Such increase in temperature ranges between 0.25°C and 1°C and peaks over 1°C in central Mali and southern Niger in the more vegetated GGW scenarios. The warming signal during the pre-monsoonal season is also reflected in the changes in temperature extremes, with an increase for the hottest and coldest day of the year between 0.3°C and 0.9°C, and more than 1.5°C, respectively, for the GGW experiments (except GGW_{LOW}) compared with the RCP-only projections. The number of tropical nights increases from 10 in the GGW_{LOW} experiment to up to more than 25 in the other GGW scenarios (Figure 4). While the GGW_{LOW} experiment does not reveal any significant cooling in the mean and extreme daily temperatures during the summer, it exhibits a clear increase in both of them in the pre-monsoonal season, leading to an increase in the hot extremes.

These results differ from those of Bamba et al.,[18] which show a cooling between February and October, peaking during the monsoon season. Diba et al.[16] and Bamba et al.[18] showed a bigger decrease in JJAS temperature (~−3°C) over the area of the project than our experiments. This is probably due to both a different interplay between albedo and evapotranspiration effects in their model and the presence of the extensive forest rather than the diversified and less-dense vegetation of our experimental design. On the other hand, Saley et al.[19]—albeit using only 14-year-long simulations—found very similar results for the hottest day of the year, suggesting this variation as a robust response.

Previous studies have, however, not considered the impact of rising temperature associated with global warming that could even offset the benefits associated with the GGW increase in rainfall over the Sahel due to increased evapotranspiration. Furthermore, the GGW vegetation would also cause an increase in humidity that may exacerbate the heat stress on the local population. In our study, we show that, albeit with higher future temperatures, the GGW enhanced rainfall and drove Sahel toward less arid conditions with slightly larger changes in the RCP2.6 than in the RCP8.5 scenario (Figure 5). In particular, Parakou in Benin moves from slightly arid to moderate humid or humid conditions in almost all experiments, while Bamako in Mali sees a shift from a semi-arid to moderately arid climate in the GGW_{HIGH} and GGW_{EXT} experiments. Southern parts of northern Africa are also affected by this increase in humid conditions, with Abuja in Nigeria moving from moderate humid to humid conditions in all experiments and Bambari moving from moderately humid to humid AI_{DM} values in the GGW_{MED} under RCP2.6 scenario, and in all GGW_{HIGH} and GGW_{EXT} experiments. With respect to human comfort, our analysis highlights the remarkable effect of the GGW on heat stress. The number of days in which the heat index is above the PD 75th and 95th percentile is further increased compared with the RCP-only scenarios between 10 and 50–60 days for all the GGW experiments. The area affected by those changes varies as a function of the vegetation density, covering a small area between southern Mali and southern Chad in the GGW_{LOW} scenario and almost the whole GGW domain in the GGW_{HIGH} and GGW_{EXT} experiments (Figures 6 and S21). The HI distributions in the Sahelian cities generally show a future increase in the mean and variance for the more extreme GGWs under both emission scenarios (Figures S23 and S24). The only exceptions are found for the capitals of Eritrea and

Ethiopia in the eastern Sahel. While the aridity index suggests an improvement in the water availability for the region due to the presence of the GGW, the increase in the HI could lead to a worsening of the habitable conditions due to the increase in heat stress on local populations as measured by the heat index.

Our results highlight the importance of the vegetation feedback and change in albedo for the northern Africa climate as suggested by previous studies,[36,37] by strengthening the WAM and triggering an increase in precipitation, depending on the density of the planted vegetation, and in temperature extremes. The discussion on the crucial aspects regarding the feasibility of the GGW project, such as the potential dynamics of the Saharan boundary and vegetation productivity limits over the Sahelian region, is still open.[40]

An important caveat of our experiment is the lack of the potential SST and dynamic vegetation feedback as both are prescribed. Indeed, several studies show the importance of both feedbacks at the interannual and interdecadal variability.[4,5,7,8,41–43] Although how vegetation is treated in the model may dominate the signal, the higher sensitivity of the other CORDEX models to anthropogenic forcing could lead them to a stronger response to GGW vegetation changes (see experimental procedures for a comparison between CORDEX and CRCM/GEM4.8). Therefore, a coordinated multi-model intercomparison of different GGW scenarios will be beneficial to constrain the local and far-afield climatic impacts of this initiative. Another potential caveat can be associated with limitations in nutrients and other mitigating factors that are not properly represented in the model. Finally, while our simulations are performed at high horizontal resolution (~13 km), the convection is still parameterized. Some studies argue that parameterized convection models show an opposite change related to the soil-vegetation feedback compared with convection-permitting models in terms of land surface forcing response.[44,45] However, Jungandreas et al.[46] showed that the response of the monsoon circulation in a convection-permitting model to an increased vegetation cover over the Sahara/Sahel region is qualitatively similar—albeit stronger—to that in parameterized convection simulations. New studies with both convection-permitting and parameterized convection models are necessary to better constrain this response also in light of the potential underestimation in our model of the GGW impacts due to the aforementioned lower sensitivity to climate change compared with CORDEX models.

As climate variability, water security, and land fertility play a notable role in achieving food security, this study provides a GGW multi-scenario experiment where different levels of vegetation density give rise to different climate impacts on the region. The findings of our study help illuminate the complex, nuanced impact of the GGW in northern Africa, revealing a mixed outcome: decreased aridity and summer temperatures alongside intensified occurrences of extreme hot days and heat indices in the pre-monsoonal season along the GGW domain. By delineating these contrasting trends, our research offers a crucial step toward understanding the multifaceted climatic consequences of the different GGW actions such as climate-smart agriculture, climatic-resilient infrastructure, and sustainable pastoralism.

Furthermore, the GGW may also affect climate far-afield (e.g., on the equatorial Atlantic and Pacific) as suggested by recent modeling studies performed under Green Sahara conditions (~6,000 years ago), showing impacts on tropical cyclones[47] and on the El Niño Southern Oscillation[48] activities. Additional studies are therefore needed to address the Wall's potential far-afield climate impacts.

In conclusion, while further studies using different climate models are necessary to better constrain the impacts of the GGW on climate, our results underscore the importance of conducting comprehensive evaluations in environmental policy planning. Acknowledging the GGW impacts becomes pivotal in steering future strategies, ensuring that the GGW ambitions align with sustainable climate goals while mitigating potential adverse effects on regional stability and ecosystem integrity in northern Africa and beyond.

EXPERIMENTAL PROCEDURES

Resource availability

Lead contact

Further information about data and code should be directed to and will be fulfilled by the lead contact, Roberto Ingrosso (ingrosso.roberto@uqam.ca).

Materials availability

This study generated no new unique materials.

Data and code availability

All codes and data to generate the figures of this study are available in the online repository: 10.5281/zenodo.10323281. The TRMM data were provided by the NASA/Goddard Space Flight Center and obtained from https://gpm.nasa.gov/missions/trmm.

Model description

We used the developmental version of the Canadian Regional Climate Model/Global Environmental Multiscale (CRCM5/GEM4.8,[23,24]) at a horizontal grid spacing of 0.12° (~13 km) and 57 vertical levels topping at 10 hPa. To have atmospheric driving data that are conformed with the ocean, we first ran global simulations on a Yin-Yang grid with the Global Environmental Multiscale (GEM) model[49] at 0.55° horizontal resolution and 73 vertical levels topping at 2 hPa GEM4.8 (the GEM version used in this study) is a fully non-hydrostatic model that uses a semi-implicit, semi-Lagrangian time discretization scheme on a horizontal Arakawa staggered C grid (see Hernández-Díaz et al.[50] for further details).

These experiments were driven by the bias-corrected SST[51] and original sea ice fraction provided by the Earth System Model of the Max-Planck-Institut für Meteorologie (MPI-ESM-MR) (https://mpimet.mpg.de/en/science.html) at the lower boundary and then used the output of those simulations to drive the regional simulations at the lateral boundary, using the same SST and sea ice fractions as for the global simulations at the lower boundary. The CRCM5/GEM4.8 lower boundary is coupled with the Canadian Land Surface Scheme[52] and an interactive lake module, FLake lake model.[53] For vegetation and land-water mask, CCI-LC vegetation and land-water mask the ESA CCI Land Cover[54] is used, while the Global Multi-resolution Terrain Elevation Data 2010 https://www.usgs.gov/coastal-changes-and-impacts/gmted2010 has been used for the model topography.

Model evaluation

A previous experiment[50] over the African CORDEX[55] domain shows that CRCM correctly detects the timing of the WAM onset over the Sahel but a dry bias is present over the region due to the southward position of the Saharan Heat Low compared with reanalyses. Consequently, the core of the AEJ is displayed slightly southward, giving rise to the above-mentioned dry bias in the region. In this study, we further evaluate CRCM/GEM4.8, by comparing it with its parental model GEM4.8[49] at 0.55° horizontal resolution, observations from the Tropical Rainfall Measuring Mission (TRMM) (10.5067/TRMM/TMPA/3H/7) and the Climate Research Unit,[56] and one reanalysis product (ERA5[57]) in terms of mean precipitation distribution for the period 2000–2019 (Figure S29). The evaluation shows a better agreement of the high-resolution model with the observations in the WAM area (West Sahel) compared with GEM4.8, although the dry bias in terms of median and lower percentiles is still present, whereas no significant change is present when considering the whole Sahelian region. To evaluate the model skills in terms of reproducing the diurnal cycle and the rainfall intermittency, we

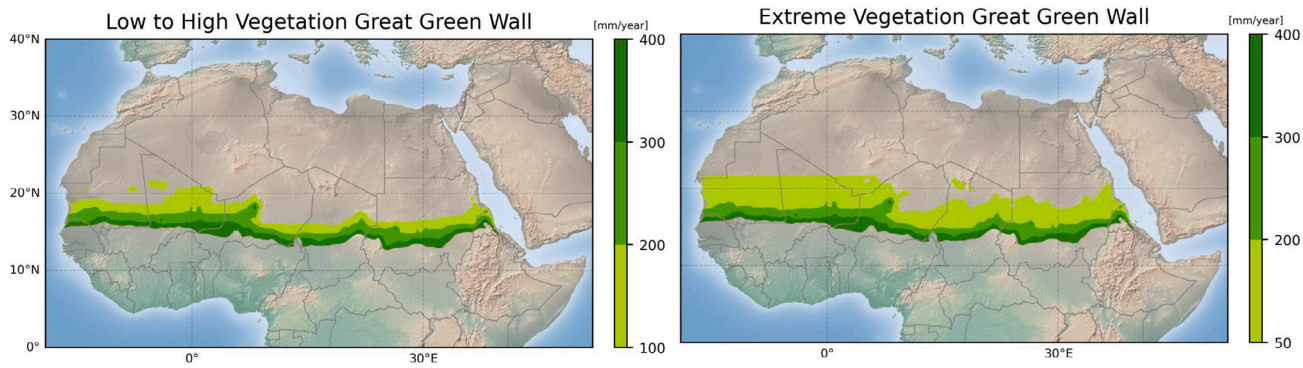

Low vegetation GGW	Medium vegetation GGW	High vegetation GGW	Extreme vegetation GGW
65% -> desert 20% -> short grass and forbs 5% -> evergreen broadleaf shrubs 10% -> deciduous shrubs	65% -> desert 20% -> short grass and forbs 5% -> evergreen broadleaf shrubs 10% -> deciduous shrubs	25% -> desert 25% -> short grass and forbs 25% -> evergreen broadleaf shrubs 25% -> deciduous shrubs	10% -> desert 25% -> short grass and forbs 30% -> evergreen broadleaf shrubs 35% -> deciduous shrubs
30% -> desert 30% -> short grass and forbs 5% -> evergreen broadleaf shrubs 15% -> deciduous shrubs 10% -> deciduous broadleaf trees 10% -> evergreen broadleaf trees	15% -> desert 20% -> short grass and forbs 10% -> evergreen broadleaf shrubs 20% -> deciduous shrubs 20% -> deciduous broadleaf trees 10% -> evergreen broadleaf trees	15% -> desert 20% -> short grass and forbs 10% -> evergreen broadleaf shrubs 20% -> deciduous shrubs 20% -> deciduous broadleaf trees 10% -> evergreen broadleaf trees	10% -> desert 15% -> short grass and forbs 15% -> evergreen broadleaf shrubs 30% -> deciduous shrubs 20% -> deciduous broadleaf trees 10% -> evergreen broadleaf trees
15% -> desert 25% -> short grass and forbs 15% -> evergreen broadleaf shrubs 15% -> deciduous shrubs 20% -> deciduous broadleaf trees 10% -> evergreen broadleaf trees	5% -> desert 15% -> short grass and forbs 15% -> evergreen broadleaf shrubs 15% -> deciduous shrubs 35% -> deciduous broadleaf trees 15% -> evergreen broadleaf trees	5% -> desert 15% -> short grass and forbs 15% -> evergreen broadleaf shrubs 15% -> deciduous shrubs 35% -> deciduous broadleaf trees 15% -> evergreen broadleaf trees	5% -> desert 15% -> short grass and forbs 15% -> evergreen broadleaf shrubs 15% -> deciduous shrubs 30% -> deciduous broadleaf trees 20% -> evergreen broadleaf trees

Figure 7. The GGW experimental design

(A) Schematic of the experimental design of the GGW, in which the prescribed vegetation type and abundance (in percent) is provided for each of climatological rainfall interval (100–200, 200–300, and 300–400 mm). Each band corresponds to a different vegetation mix of woody and herbaceous species, according to the official GGW plans from the Pan African Agency of the Great Green Wall. (B) Extreme case, where the first rainfall interval starts at 50 mm. The percentage of desert and nude soil over the GGW area in the PD simulation is 72% while it is around 40%, 33%, 16%, and 8% in the GGWs experiments from low to extreme, respectively.

compared GEM/CRCM4.8 3-hourly data with TRMM. In terms of the diurnal cycle (Figure S30), the model clearly underestimates rainfall compared with the satellite observations. A maximum peak over the whole Sahel of 5 mm/day is found for TRMM at midnight, whereas a peak of 2.68 mm/day (3.8 mm/day over the western Sahel) is shown for GEM/CRCM4.8 at 9 p.m. A minimum rainfall is detected at noon over the whole Sahel of about 1.91 mm/day for TRMM and 1.5 mm/day for GEM/CRCM4.8, while the model minimum rainfall is closer to observations over the western Sahel with 2.11 mm/day at 3 p.m. and 2.36 mm/day at noon, respectively. However, the general diurnal cycle pattern is well reproduced, with maximum precipitation during the early night and minimum precipitation during the middle of the day. As expected, the model diurnal cycle over the western Sahel is closer to observations compared with that for the whole Sahel region, as also seen in the mean precipitation boxplots (Figure S29).

In terms of CDDs, the model distributions of annual CDDs show a similar behavior compared with TRMM, with peaks of 250 days in both datasets (Figure S31). Over West Sahel, the CDD model distribution slightly moves toward a bit longer CDD. Both datasets are characterized by a maximum CDD of about 3,400 days.

The experimental design

A total of 11 simulations had been performed for two distinct 30-year periods (Table S2). Three simulations without the GGW had been carried out and considered as reference cases: one under the present climate (1990–2019) and two under RCP2.6 and RCP8.5[25] future scenarios (2071–2100). RCP8.5 is the high emission scenario that better reproduces the recent CO_2 emissions,[58] even though its emission trajectory could become less likely in the future, given the current policies.[59] In addition, a total of eight sensitivity experiments under the two future scenarios were carried out considering four different levels of vegetation density. The four levels have been named GGW_{LOW}, GGW_{MED}, GGW_{HIGH}, and GGW_{EXT} (Figure 7). GGW_{LOW} and GGW_{MED} are characterized by a total percentage of desert in the GGW region (100–400 mm) of 40% and 33%, respectively, whereas GGW_{HIGH}, and GGW_{EXT} show a percentage of 16%, and 8%, respectively (Figure S1). The referenced present-day (PD) simulation presents a percentage of desert and nude soil of 72% over the GGW region between 100 and 400 mm. The chosen type of vegetation agrees with the species considered in the main documents produced by the PAGGW[11] such as *Acacia senegal*, *Acacia nilotica*, and *Balanites aegyptiaca*. No change in previous land cover categories such as urban, swamp or crops had been made because of the difficulty of evaluating the future evolution of these categories. More in detail, in GGW_{LOW}, we shifted northward the desert fraction as present in the model scheme: the 100–200 mm desert fraction is replaced by the 200–300 mm fraction, the 200–300 mm fraction is replaced by the 300–400 mm fraction, and the 300–400 mm fraction by that from the 400 to 500 mm fraction. Thirty percent of trees are present in the third band (300–400 mm). GGW_{MED} has the same GGW_{LOW} mix of vegetation for the first band with 65% of desert, while sharing the same mix of vegetation in the other two bands with GGW_{HIGH} where the percentage of trees in the third band moves to 50%. GGW_{HIGH} sees a percentage of 25% of desert in the first band. In the extreme case, a percentage of 10% of desert is present in the first two bands (50–300 mm), moving to 5% in the third one. Finally, in GGW_{EXT} experiment, the percentage of trees in the third band is still 50% but with a higher concentration of evergreen broadleaf trees compared with GGW_{MED} and GGW_{HIGH}. In the introduction, we mentioned that in previous studies the pre-existent vegetation had been

replaced with a uniform evergreen forest over different latitudinal bands over the region. Although these studies do not provide values for the modification in albedo, rainforests have an albedo of the order of 0.12–0.13[60] while in our case the albedo ranges between 0.15 and 0.3 (Figure S15). Such albedo difference can play a critical role in altering the WAM dynamics.[61]

Climate extreme indices

Climate indices play an important role in monitoring the potential risks and damages of climate change. The definition of these indicators looks at the tails of the parameter distribution, which reflect the change in the extreme events. Consequently, the use of different temperature and precipitation climate extreme indices was here considered as defined by the Expert Team on Climate Change Detection and Indices (ETCCDI).[62,63] A set of indicators from the 27 ETCDDI had been considered (Table S3) in order to have a good representation of extreme temperature, precipitation, and dry spells over the area. For the temperature we calculated the annual extreme of daily maximum and minimum temperature (TXx and TNn, respectively), and the number of nights with daily minimum temperature above 20°C (tropical nights [TR20]). As a measure of the longest yearly dry spells, we considered the CDDs, the maximum number of consecutive days with precipitation lower than 1 mm. Finally, the annual maximum of the precipitation amount fell in 5 consecutive days (RX5), the annual total precipitation from days with an amount of precipitation above the 95th percentile (very wet days, R95p), and the number of days per year in which the daily precipitation exceeds 1 mm (rainy days, RR1mm) were considered to show potential changes in heavy precipitation.

Statistical analysis

For the statistical evaluation of the differences, two statistical tests were used: a two-tailed Student's t test[64] for temperature, assuming a normal distribution for this parameter and the non-parametric Wilcoxon signed-rank test[65] for parameters such as precipitation or wind, where the normal assumption is not possible. The considered level of significance is 5% for both tests.

The WAM length and the AEWs

The monsoon's length is defined as the time between the onset and the withdrawal of the monsoon. The computation of the onset is based on Sultan and Janicot.[66] An empirical orthogonal function (EOF) analysis was performed on the zonally averaged daily rainfall data from March to November over the area between 15°W–15°E and 0°N–30°N. The zonally averaged daily rainfall time series at the maximum of the first mode (EOF1) was then filtered to remove variability below 10 days with a 10-day running mean. The monsoon's onset was defined as the date preceding the largest increase in precipitation over a 20-day period. Finally, the withdrawal was defined as the date on which the zonally averaged precipitation at 10.5°N falls below 2 mm/day for at least 20 consecutive days.[67]

The AEWs are westward-propagating disturbances with wavelengths of approximately 3,000–4,000 km, a propagation speed of about 8 m/s,[68,69] and a period of around 3–5 days. AEWs play a role in the initiation and organization of the mesoscale convective systems, which are the main contributors to the Sahelian rainfall. In this study, we detected the AEW activity by filtering the daily means of the meridional wind between June and September (JJAS) with a 2- to 6-day band-pass filter.[70]

Aridity index

In this study, the AI_{DM} (De Martonne[38]) was used to evaluate changes in aridity and water availability over the region. The AI_{DM} is a simplified index, defined as a function of the annual mean temperature and precipitation, which provides similar results to other aridity indices present in the scientific literature (see Paniagua and co-workers[71,72] for further details). Here, we defined a new category, desert, for aridity index values lower than 5. This category properly distinguishes the desertic climate (Figure 5), facilitating the purpose of our analysis regarding potential changes in local climate, characterized by high arid conditions. Specifically, the De Martonne index is defined as:

$$AI_{DM} = \frac{P}{T+10} \qquad \text{(Equation 1)}$$

where P is the annual mean precipitation and T is the annual mean temperature in degrees Celsius at the reference height (2 m).

HI

The HI calculation is based on Rothfusz's regression equation (https://www.weather.gov/media/ffc/ta_htindx.PDF):

$$\begin{aligned} HI = {} & 42.379 + 2.04901523 * T + 10.14333127 * RH - 0.22475541 * \\ & T * RH - 0.00683783 * T * T - 0.05481717 * RH * RH \\ & + 0.00122874 * T * T * RH + 0.00085282 * T * RH * RH \\ & - 0.00000199 * T * T * RH * RH \end{aligned} \qquad \text{(Equation 2)}$$

where T is the surface temperature in degrees Fahrenheit and RH is the percentage of relative humidity. The HI is converted into degrees Celsius and has an error of ±1.3°F (±0.7°C). Some adjustments are applied to the index (when RH is less than 13% and the temperature is between 80°C and 112°C, or RH is greater than 85% and the temperature is between 80°C and 87°C), following the instructions of the National Oceanic and Atmospheric Administration/National Weather Service (see https://www.wpc.ncep.noaa.gov/html/heatindex_equation.shtml).

SUPPLEMENTAL INFORMATION

Supplemental information can be found online at https://doi.org/10.1016/j.oneear.2024.01.017.

ACKNOWLEDGMENTS

The authors thank Katja Winger for helping set up the model simulations and for helpful ideas and discussions; Roberto Salustri, Scientific Director of Reseda ONLUS (ecoistituto@resedaweb.org), for useful information for the experimental design regarding local GGW actions in northern Senegal; and Dr. Leonardo Bagaglini for precious suggestions and help with satellite data. The authors are grateful to Federica Ferri for her precious support with the graphical abstract. We also thank the Recherche en Prévision Numérique (RPN), the Meteorological Research Branch (MRB), and the Canadian Meteorological Center (CMC) for permission to use the GEM model as the basis for our CRCM. We thank the World Climate Research Program's Working Group on Regional Climate, and the Working Group on Coupled Modeling, former coordinating body of CORDEX and the climate modeling groups (listed in Table S1 of this paper). We also acknowledge the Earth System Grid Federation infrastructure, an international effort led by the US Department of Energy's Program for Climate Model Diagnosis and Intercomparison, the European Network for Earth System Modeling, and other partners in the Global Organization for Earth System Science Portals (GO-ESSP) that allow to download CORDEX data used for the validation. Finally, this study would not have been possible without access to valuable data such as the MPI-ESM-MR model output to drive the GEM global simulations. This research was enabled in part by support provided by the Digital Research Alliance of Canada (https://alliancecan.ca) and Calcul Quebec (https://www.calculquebec.ca). This research has been supported by the Natural Sciences and Engineering Research Council of Canada (NSERC grant no. RGPIN-2018-04981) and NOVA - FRQNT-NSERC program (ALLRP 577112-22 and 2023-NOVA-324826).

AUTHOR CONTRIBUTIONS

Conceptualization, R.I. and F.S.R.P.; methodology, R.I. and F.S.R.P.; experiments, R.I.; data analysis, R.I.; writing – original draft, R.I.; writing – review & editing, R.I. and F.S.R.P.; funding acquisition, F.S.R.P.

DECLARATION OF INTERESTS

The authors declare no competing interests.

Received: November 15, 2022
Revised: October 17, 2023
Accepted: January 22, 2024
Published: February 14, 2024

REFERENCES

1. Diffenbaugh, N.S., and Giorgi, F. (2012). Climate change hotspots in the CMIP5 global climate model ensemble. Climatic Change *114*, 813–822. https://doi.org/10.1007/s10584-012-0570-x.
2. Turco, M., Palazzi, E., von Hardenberg, J., and Provenzale, A. (2015). Observed climate change hotspots. Geophys. Res. Lett. *42*, 3521–3528. https://doi.org/10.1002/2015GL063891.
3. Dilley, J., Chen, R.S., Deichmann, U., Lerner-Lam, A.L., Arnold, M., Agwe, J., Buys, P., Kjekstad, O., Lyon, B., and Yetman, G. (2005). Natural Disaster Hotspots: A Global Risk Analysis (World Bank).
4. Folland, C.K., Palmer, T.N., and Parker, D.E. (1986). Sahel rainfall and worldwide sea temperatures, 1901–85. Nature *320*, 602–607. https://doi.org/10.1038/320602a0.
5. Janicot, S., Moron, V., and Fontaine, B. (1996). Sahel droughts and Enso dynamics. Geophys. Res. Lett. *23*, 515–518. https://doi.org/10.1029/96GL00246.
6. Giannini, A., Saravanan, R., and Chang, P. (2003). Oceanic Forcing of Sahel Rainfall on Interannual to Interdecadal Time Scales. Science *302*, 1027–1030. https://doi.org/10.1126/science.1089357.
7. Biasutti, M., Held, I.M., Sobel, A.H., and Giannini, A. (2008). SST Forcings and Sahel Rainfall Variability in Simulations of the Twentieth and Twenty-First Centuries. J. Clim. *21*, 3471–3486. https://doi.org/10.1175/2007JCLI1896.1.
8. Charney, J.G. (1975). Dynamics of deserts and drought in the Sahel. Q. J. R. Meteorol. Soc. *101*, 193–202. https://doi.org/10.1002/qj.49710142802.
9. Giannini, A., and Kaplan, A. (2019). The role of aerosols and greenhouse gases in Sahel drought and recovery. Clim. Change *152*, 449–466. https://doi.org/10.1007/s10584-018-2341-9.
10. Zeng, N. (2003). Drought in the Sahel. Science *302*, 999–1000. https://doi.org/10.1126/science.1090849.
11. PAGGW (2018). Initiative de la Grande Muraille Verte: realisations 2011-2017 et defis sur la trajectoire 2030 (Les echos de la GMV).
12. Turner, M.D., Carney, T., Lawler, L., Reynolds, J., Kelly, L., Teague, M.S., and Brottem, L. (2021). Environmental rehabilitation and the vulnerability of the poor: The case of the Great Green Wall. Land Use Pol. *111*, 105750. https://doi.org/10.1016/j.landusepol.2021.105750.
13. Goffner, D., Sinare, H., and Gordon, L.J. (2019). The Great Green Wall for the Sahara and the Sahel Initiative as an opportunity to enhance resilience in Sahelian landscapes and livelihoods. Reg. Environ. Change *19*, 1417–1428. https://doi.org/10.1007/s10113-019-01481-z.
14. Ornstein, L., Aleinov, I., and Rind, D. (2009). Irrigated afforestation of the Sahara and Australian Outback to end global warming. Climatic Change *97*, 409–437. https://doi.org/10.1007/s10584-009-9626-y.
15. Abiodun, B.J., Adeyewa, Z.D., Oguntunde, P.G., Salami, A.T., and Ajayi, V.O. (2012). Modeling the impacts of reforestation on future climate in West Africa. Theor. Appl. Climatol. *110*, 77–96. https://doi.org/10.1007/s00704-012-0614-1.
16. Diba, I., Camara, M., and Sarr, A.B. (2016). Impacts of the Sahel-Sahara Interface Reforestation on West African Climate: Intraseasonal Variability and Extreme Precipitation Events. Adv. Meteorol. *2016*, 1–20. https://doi.org/10.1155/2016/3262451.
17. Kemena, T.P., Matthes, K., Martin, T., Wahl, S., and Oschlies, A. (2018). Atmospheric feedbacks in North Africa from an irrigated, afforested Sahara. Clim. Dyn. *50*, 4561–4581. https://doi.org/10.1007/s00382-017-3890-8.
18. Bamba, A., Diallo, I., Touré, N.E., Kouadio, K., Konaré, A., Dramé, M.S., Diedhiou, A., Silué, S., Doumbia, M., and Tall, M. (2019). Effect of the African greenbelt position on West African summer climate: a regional climate modeling study. Theor. Appl. Climatol. *137*, 309–322. https://doi.org/10.1007/s00704-018-2589-z.
19. Saley, I.A., Salack, S., Sanda, I.S., Moussa, M.S., Bonkaney, A.L., Ly, M., and Fodé, M. (2019). The possible role of the Sahel Greenbelt on the occurrence of climate extremes over the West African Sahel. Atmos. Sci. Lett. *20*, e927. https://doi.org/10.1002/asl.927.
20. Mathon, V., Laurent, H., and Lebel, T. (2002). Mesoscale Convective System Rainfall in the Sahel. J. Appl. Meteorol. *41*, 1081–1092. https://doi.org/10.1175/1520-0450(2002)041<1081:MCSRIT>2.0.CO;2.
21. Lebel, T., Diedhiou, A., and Laurent, H. (2003). Seasonal cycle and interannual variability of the Sahelian rainfall at hydrological scales. J. Geophys. Res. *108*. https://doi.org/10.1029/2001JD001580.
22. Nicholson, S.E. (2013). The West African Sahel: A Review of Recent Studies on the Rainfall Regime and Its Interannual Variability. ISRN Meteorology *2013*. 453521–32. https://doi.org/10.1155/2013/453521.
23. Girard, C., Plante, A., Desgagné, M., McTaggart-Cowan, R., Côté, J., Charron, M., Gravel, S., Lee, V., Patoine, A., Qaddouri, A., et al. (2014). Staggered Vertical Discretization of the Canadian Environmental Multiscale (GEM) Model Using a Coordinate of the Log-Hydrostatic-Pressure Type. Mon. Weather Rev. *142*, 1183–1196. https://doi.org/10.1175/MWR-D-13-00255.1.
24. McTaggart-Cowan, R., Vaillancourt, P.A., Zadra, A., Chamberland, S., Charron, M., Corvec, S., Milbrandt, J.A., Paquin-Ricard, D., Patoine, A., Roch, M., et al. (2019). Modernization of Atmospheric Physics Parameterization in Canadian NWP. J. Adv. Model. Earth Syst. *11*, 3593–3635. https://doi.org/10.1029/2019MS001781.
25. Moss, R.H., Edmonds, J.A., Hibbard, K.A., Manning, M.R., Rose, S.K., van Vuuren, D.P., Carter, T.R., Emori, S., Kainuma, M., Kram, T., et al. (2010). The next generation of scenarios for climate change research and assessment. Nature *463*, 747–756. https://doi.org/10.1038/nature08823.
26. Klutse, N.A.B., Ajayi, V.O., Gbobaniyi, E.O., Egbebiyi, T.S., Kouadio, K., Nkrumah, F., Quagraine, K.A., Olusegun, C., Diasso, U., Abiodun, B.J., et al. (2018). Potential impact of 1.5°C and 2°C global warming on consecutive dry and wet days over West Africa. Environ. Res. Lett. *13*, 055013. https://doi.org/10.1088/1748-9326/aab37b.
27. Diedhiou, A., Bichet, A., Wartenburger, R., Seneviratne, S.I., Rowell, D.P., Sylla, M.B., Diallo, I., Todzo, S., Touré, N.E., Camara, M., et al. (2018). Changes in climate extremes over West and Central Africa at 1.5°C and 2°C global warming. Environ. Res. Lett. *13*, 065020. https://doi.org/10.1088/1748-9326/aac3e5.
28. Dosio, A., Lennard, C., and Spinoni, J. (2022). Projections of indices of daily temperature and precipitation based on bias-adjusted CORDEX-Africa regional climate model simulations. Clim. Change *170*, 13. https://doi.org/10.1007/s10584-022-03307-0.
29. Dosio, A., Jury, M.W., Almazroui, M., Ashfaq, M., Diallo, I., Engelbrecht, F.A., Klutse, N.A.B., Lennard, C., Pinto, I., Sylla, M.B., and Tamoffo, A.T. (2021). Projected future daily characteristics of African precipitation based on global (CMIP5, CMIP6) and regional (CORDEX, CORDEX-CORE) climate models. Clim. Dyn. *57*, 3135–3158. https://doi.org/10.1007/s00382-021-05859-w.
30. Seneviratne, S.I., Zhang, X., Adnan, M., Badi, W., Dereczynski, C., Di Luca, A., Ghosh, S., Iskandar, I., Kossin, J., Lewis, S., Otto, F., et al. (2021). Weather and Climate Extreme Events in a Changing Climate. In Climate Change 2021: The Physical Science Basis (Climate Change). https://doi.org/10.1017/9781009157896.013.
31. Kendon, E.J., Stratton, R.A., Tucker, S., Marsham, J.H., Berthou, S., Rowell, D.P., and Senior, C.A. (2019). Enhanced future changes in wet and dry extremes over Africa at convection-permitting scale. Nat. Commun. *10*, 1794. https://doi.org/10.1038/s41467-019-09776-9.
32. Newell, R.E., and Kidson, J.W. (1984). African mean wind changes between Sahelian wet and dry periods. J. Climatol. *4*, 27–33. https://doi.org/10.1002/joc.3370040103.
33. Shekhar, R., and Boos, W.R. (2017). Weakening and Shifting of the Saharan Shallow Meridional Circulation during Wet Years of the West African Monsoon. J. Clim. *30*, 7399–7422. https://doi.org/10.1175/JCLI-D-16-0696.1.
34. Nicholson, S.E., Barcilon, A.I., Challa, M., and Baum, J. (2007). Wave Activity on the Tropical Easterly Jet. J. Atmos. Sci. *64*, 2756–2763. https://doi.org/10.1175/JAS3946.1.

35. Thorncroft, C.D., Hall, N.M.J., and Kiladis, G.N. (2008). Three-Dimensional Structure and Dynamics of African Easterly Waves. Part III: Genesis. J. Atmos. Sci. *65*, 3596–3607. https://doi.org/10.1175/2008JAS2575.1.

36. Kutzbach, J., Bonan, G., Foley, J., and Harrison, S.P. (1996). Vegetation and soil feedbacks on the response of the African monsoon to orbital forcing in the early to middle Holocene. Nature *384*, 623–626. https://doi.org/10.1038/384623a0.

37. Messori, G., Gaetani, M., Zhang, Q., Zhang, Q., and Pausata, F.S.R. (2019). The water cycle of the mid-Holocene West African monsoon: The role of vegetation and dust emission changes. Int. J. Climatol. *39*, 1927–1939. https://doi.org/10.1002/joc.5924.

38. De Martonne, E. (1926). Aréisme et Indice d'aridité. Comptes Rendus de L'Academy of Science *182*, 1395–1398. https://doi.org/10.1002/qj.49707130905.

39. Turner, M.D., Davis, D.K., Yeh, E.T., Hiernaux, P., Loizeaux, E.R., Fornof, E.M., Rice, A.M., and Suiter, A.K. (2023). Great Green Walls: Hype, Myth, and Science. Annu. Rev. Environ. Resour. *48*, 263–287. https://doi.org/10.1146/annurev-environ-112321-111102.

40. Elagib, N.A., Khalifa, M., Babker, Z., Musa, A.A., and Fink, A.H. (2021). Demarcating the rainfed unproductive zones in the African Sahel and Great Green Wall regions. Land Degrad. Dev. *32*, 1400–1411. https://doi.org/10.1002/ldr.3793.

41. Zeng, N., Neelin, J.D., Lau, K., and Tucker, C.J. (1999). Enhancement of Interdecadal Climate Variability in the Sahel by Vegetation Interaction. Science *286*, 1537–1540. https://doi.org/10.1126/science.286.5444.1537.

42. Giannini, A., Salack, S., Lodoun, T., Ali, A., Gaye, A.T., and Ndiaye, O. (2013). A unifying view of climate change in the Sahel linking intra-seasonal, interannual and longer time scales. Environ. Res. Lett. *8*, 024010. https://doi.org/10.1088/1748-9326/8/2/024010.

43. Rodríguez-Fonseca, B., Mohino, E., Mechoso, C.R., Caminade, C., Biasutti, M., Gaetani, M., Garcia-Serrano, J., Vizy, E.K., Cook, K., Xue, Y., et al. (2015). Variability and Predictability of West African Droughts: A Review on the Role of Sea Surface Temperature Anomalies. J. Clim. *28*, 4034–4060. https://doi.org/10.1175/JCLI-D-14-00130.1.

44. Hohenegger, C., Brockhaus, P., Bretherton, C.S., and Schär, C. (2009). The Soil Moisture–Precipitation Feedback in Simulations with Explicit and Parameterized Convection. J. Clim. *22*, 5003–5020. https://doi.org/10.1175/2009JCLI2604.1.

45. Taylor, C.M., Birch, C.E., Parker, D.J., Dixon, N., Guichard, F., Nikulin, G., and Lister, G.M.S. (2013). Modeling soil moisture-precipitation feedback in the Sahel: Importance of spatial scale versus convective parameterization. Geophys. Res. Lett. *40*, 6213–6218. https://doi.org/10.1002/2013GL058511.

46. Jungandreas, L., Hohenegger, C., and Claussen, M. (2023). How does the explicit treatment of convection alter the precipitation–soil hydrology interaction in the mid-Holocene African humid period? Clim. Past *19*, 637–664. https://doi.org/10.5194/cp-19-637-2023.

47. Pausata, F.S.R., Zhang, Q., Muschitiello, F., Lu, Z., Chafik, L., Niedermeyer, E.M., Stager, J.C., Cobb, K.M., and Liu, Z. (2017). Greening of the Sahara suppressed ENSO activity during the mid-Holocene. Nat. Commun. *8*, 16020. https://doi.org/10.1038/ncomms16020.

48. Pausata, F.S.R., Emanuel, K.A., Chiacchio, M., Diro, G.T., Zhang, Q., Sushama, L., Stager, J.C., and Donnelly, J.P. (2017). Tropical cyclone activity enhanced by Sahara greening and reduced dust emissions during the African Humid Period. Proc. Natl. Acad. Sci. USA *114*, 6221–6226. https://doi.org/10.1073/pnas.1619111114.

49. Côté, J., Gravel, S., Méthot, A., Patoine, A., Roch, M., and Staniforth, A. (1998). The Operational CMC-MRB Global Environmental Multiscale (GEM) Model. Part I: Design Considerations and Formulation. Mon. Weather Rev. *126*, 1373–1395. https://doi.org/10.1175/1520-0493(1998)126<1373:TOCMGE>2.0.CO;2.

50. Hernández-Díaz, L., Laprise, R., Sushama, L., Martynov, A., Winger, K., and Dugas, B. (2013). Climate simulation over CORDEX Africa domain using the fifth-generation Canadian Regional Climate Model (CRCM5). Clim. Dyn. *40*, 1415–1433. https://doi.org/10.1007/Fs00382-012-1387-z.

51. Hernández-Díaz, L., Nikiéma, O., Laprise, R., Winger, K., and Dandoy, S. (2019). Effect of empirical correction of sea-surface temperature biases on the CRCM5-simulated climate and projected climate changes over North America. Clim. Dyn. *53*, 453–476. https://doi.org/10.1007/s00382-018-4596-2.

52. Verseghy, D.L. (2000). The Canadian land surface scheme (CLASS): Its history and future. Atmos.-Ocean *38*, 1–13. https://doi.org/10.1080/07055900.2000.9649637.

53. Mironov, D., Heise, E., Kourzeneva, E., Ritter, B., Schneider, N., and Terzhevik, A. (2010). Implementation of the lake parameterisation scheme FLake into the numerical weather prediction model COSMO. Boreal Environ Resw *15*, 218–230.

54. ESA (2017). Land Cover CCI Product User Guide Version 2. ESA. Available from. maps.elie.ucl.ac.be/CCI/viewer/download/ESACCI-LC-Ph2-PUGv2_2.0.pdf.

55. Giorgi, F., Jones, C., and Asrar, G. (2009). Addressing Climate Information Needs at the Regional Level: The CORDEX Framework (World Meteorological Organization). Available from. https://cordex.org/wp-content/uploads/2012/11/cordex_giorgi_wmo-1.pdf.

56. Harris, I., Osborn, T.J., Jones, P., and Lister, D. (2020). Version 4 of the CRU TS monthly high-resolution gridded multivariate climate dataset. Sci. Data *7*, 109.

57. Hersbach, H., Bell, B., Berrisford, P., Hirahara, S., Horányi, A., Muñoz-Sabater, J., Nicolas, J., Peubey, C., Radu, R., Schepers, D., et al. (2020). The ERA5 global reanalysis. Q. J. R. Meteorol. Soc. *146*, 1999–2049. https://doi.org/10.1002/qj.3803.

58. Schwalm, C.R., Glendon, S., and Duffy, P.B. (2020). RCP8.5 tracks cumulative CO2 emissions. Proc. Natl. Acad. Sci. USA *117*, 19656–19657. https://doi.org/10.1073/pnas.2007117117.

59. Hausfather, Z., and Peters, G.P. (2020). Emissions – the 'business as usual' story is misleading. Nature *577*, 618–620. https://doi.org/10.1038/d41586-020-00177-3.

60. Giambelluca, T.W., Hölscher, D., Bastos, T.X., Frazão, R.R., Nullet, M.A., and Ziegler, A.D. (1997). Observations of Albedo and Radiation Balance over Postforest Land Surfaces in the Eastern Amazon Basin. J. Clim. *10*, 919–928. https://doi.org/10.1175/1520-0442(1997)010<0919:OOAARB>2.0.CO;2.

61. Pausata, F.S., Gaetani, M., Messori, G., Berg, A., Maia de Souza, D., Sage, R.F., and deMenocal, P.B. (2020). The Greening of the Sahara: Past Changes and Future Implications. One Earth *2*, 235–250. https://doi.org/10.1016/j.oneear.2020.03.002.

62. Frich, P., Alexander, L.V., Della Marta, P., Gleason, B., Haylock, M., Klein Tank, A.M.G., and Peterson, T. (2002). Observed coherent changes in climatic extremes during the second half of the twentieth century. Clim. Res. *19*, 193–212. https://doi.org/10.3354/cr019193.

63. Zhang, X., Alexander, L., Hegerl, G.C., Jones, P., Tank, A.K., Peterson, T.C., Trewin, B., and Zwiers, F.W. (2011). Indices for monitoring changes in extremes based on daily temperature and precipitation data. WIREs Climate Change *2*, 851–870. https://doi.org/10.1002/wcc.147.

64. Yuen, K.K., and Dixon, W.J. (1973). The Approximate Behaviour and Performance of the Two-Sample Trimmed t. Biometrika *60*, 369–374.

65. Wilcoxon, F. (1945). Individual Comparisons by Ranking Methods. Biometrics Bulletin *1*, 80–83.

66. Sultan, B., and Janicot, S. (2003). The West African Monsoon Dynamics. Part II: The "Preonset" and "Onset" of the Summer Monsoon. J. Clim. *16*, 3407–3427. https://doi.org/10.1175/1520-0442(2003)016<3407:TWAMDP>2.0.CO;2.

67. Zhang, G., and Cook, K.H. (2014). West African monsoon demise: Climatology, interannual variations, and relationship to seasonal rainfall. JGR. Atmospheres *119*, 175–210. 193. https://doi.org/10.1002/2014JD022043.

68. Paradis, D., Lafore, J.P., Redelsperger, J.L., and Balaji, V. (1995). African Easterly Waves and Convection. Part I: Linear Simulations. J. Atmos. Sci. *52*, 1657–1679. https://doi.org/10.1175/1520-0469(1995)052<1657:AEWACP>2.0.CO;2.

69. Diedhiou, A., Janicot, S., Viltard, A., de Felice, P., and Laurent, H. (1999). Easterly wave regimes and associated convection over West Africa and tropical Atlantic: results from the NCEP/NCAR and ECMWF reanalyses. Clim. Dynam. *15*, 795–822. https://doi.org/10.1007/s003820050316.

70. Skinner, C.B., and Diffenbaugh, N.S. (2014). Projected Changes in African Easterly Wave Intensity and Track in Response to Greenhouse Forcing. Proc. Natl. Acad. Sci. USA *111*, 6882–6887. https://doi.org/10.1002/jgrd.50363.

71. Paniagua, L., García-Martín, A., Moral, F., and Rebollo, F. (2019). Aridity in the Iberian Peninsula (1960–2017): distribution, tendencies, and changes. Theor. Appl. Climatol. *138*, 811–830. https://doi.org/10.1007/s00704-019-02866-0.

72. Sohoulande, C.D.D., Awoye, H., Nouwakpo, K.S., Dogan, S., Szogi, A.A., Stone, K.C., and Martin, J.H. (2022). A Global-Scale Assessment of Water Resources and Vegetation Cover Dynamics in Relation with the Earth Climate Gradient. Remote Sens. Earth Syst. Sci. *5*, 193–206. https://doi.org/10.1007/s41976-021-00063-0.